

CHARACTERIZATION OF THE INLET FLOW CONDITIONS FOR THE  
MODERATOR TEST FACILITY



CHARACTERIZATION OF THE INLET FLOW CONDITIONS FOR THE  
MODERATOR TEST FACILITY

By CHRISTOPHER W. HOLLINGSHEAD, B.Eng

A Thesis

Submitted to the School of Graduate Studies

In partial Fulfillment of the Requirements for the Degree

Master of Applied Science

McMaster University

© Christopher Hollingshead, June 2017

MASTER OF APPLIED SCIENCE (2017)

MCMASTER UNIVERSITY

(Engineering Physics)

Hamilton, Ontario, Canada

Title: CHARACTERIZATION OF THE INLET FLOW CONDITIONS FOR  
MODERATOR TEST FACILITY

Author: Christopher William Hollingshead, B.Eng (McMaster University)

Supervisor: Dr. D.R. Novog

Number of Pages: xiv, 109

## **ACKNOWLEDGEMENTS**

I could not have accomplished this work without the guidance and support of my supervisor Dr. Novog. You taught me a lot of valuable technical and life lessons and I am very grateful.

I would also like to extend my gratitude to Dr. Rashkovan, you always managed to find a mistake I made. Thank you for all of your time and guidance, I learned a lot.

I would also like to thank Jim Cleaver and Clealand Berwick from the Machine shop. You all taught me a great deal and helped me more than you had to.

I'd like to acknowledge my fellow students and summer students who helped me tremendously. In particular I'd like to thank Garik, Kendall, James, Mengmeng, Changrui, Dion, Liz, Jared and Andrew for helping to keep me sane and for putting up with me.

Finally, I could not have done anything without the support of my loving family and all that they have done for me to help get to this point. Thank you all.

## **ABSTRACT**

Flow in the Moderator of a CANDU reactor can be very complex due to the interplay of convective and buoyant effects. Experiments have been performed to measure temperature and velocity fields for these kind of flows, although concerns still exist. As a result a Moderator test facility has been built in order to validate CFD models for future predictions and safety analysis. To properly validate this experiment an accurate set of inlet flow conditions must be established in order to ensure a fair comparison.

A series of flow conditions indicative of the header assemblies which feed flow into the moderator test facility have been investigated through experimentation, empirical evaluation and numerical simulation. They include flow through curved tubes, turbulent free jets and flow through dividing manifolds. The goal of the present study is to establish the modelling approach to predict the flow distribution inside the manifold and velocity field out of the J-nozzles.

A variety of RANS based turbulence models and computational meshes were employed in the numerical study. The turbulence model that was found to perform best was the realizable  $k$ - $\epsilon$  model. It was also found that the velocity field of the J-nozzles is constant between Reynolds numbers of 6800-9300. These Reynolds numbers are indicative of those expected out of the header assemblies.

## Table of Contents

I.	List of Figures .....	vii
II.	List of Tables .....	xi
III.	List of Variables.....	xii
1	INTRODUCTION .....	1
1.1	CANDU Moderator.....	2
1.2	Computational Fluid Dynamics .....	6
1.2.1	Finite Volume Method.....	6
1.2.2	Turbulence Modelling.....	7
1.2.3	Wall Modelling.....	13
2	LITERATURE REVIEW .....	15
2.1	Manifolds .....	16
2.2	Flow in bends .....	21
2.3	Turbulent Round Jets .....	22
3	RESULTS .....	23
3.1	Flow through Bent Circular Tubes.....	23
3.1.1	Experimental Setup of Sudo et al (1998).....	24
3.1.2	CFD Setup for the Bend.....	25

3.1.3	Comparison to Experiment and Separate Numerical Study .....	31
3.2	Header Assembly Tests .....	37
3.2.1	Geometry Setup .....	38
3.2.2	Experiment Setup.....	39
3.2.3	Experimental Results .....	40
3.2.4	Discrete Calculation Model .....	42
3.2.5	Header Assembly CFD Setup.....	43
3.2.6	Comparison to Experiment .....	48
3.2.7	Impact of Discharge Port Diameter Tolerances.....	49
3.2.8	Validation of Models .....	51
3.3	J-Nozzles .....	55
3.3.1	Experiment Setup.....	55
3.3.2	Results and Repeatability.....	62
3.3.3	Effects of Flow Rate .....	68
3.3.4	CFD Setup.....	70
3.3.5	Comparison to Experiment .....	79
4	FUTURE WORK.....	83
4.1	Improved Nozzle Velocity Field Measurements.....	83
4.2	Additional Separate Effects Study .....	84

4.3	Simulation of Additional Header Assemblies .....	84
5	CONCLUSIONS.....	85
6	Bibliography .....	87
7	Appendix.....	92
7.1	Additional J-Nozzle PIV Data.....	92
7.2	Experimental Pipe Jet Study .....	95
7.2.1	Experimental Setup.....	96
7.3	Header Assembly Drawings.....	100
7.4	PIV Standard Operating Procedure .....	106

## **I. List of Figures**

Figure 1:	Displays CANDU reactor calandria and other components from [1] .....	2
Figure 2:	Isometric of Moderator Test Facility.....	4
Figure 3:	Header Assembly for the Moderator Test Facility (bottom left), manifold (top) and J-Nozzle (right) .....	5
Figure 4:	Displays discretization of domain .....	6
Figure 5:	Displays Control Volumes around points W, E and P .....	7
Figure 6:	Isometric of Header Assembly .....	16
Figure 7:	Displays Manifold Branches and Discharge Ports .....	17

Figure 8: Displays the pressure increase in the main channel of a manifold after a discharge port from [10] .....	19
Figure 9: Sudo et al (1998) Experimental Setup [17] .....	24
Figure 10: Sudo et al (1998) Measurement Grid [17].....	25
Figure 11: Grid for the 90° bend .....	26
Figure 12: Wall Y+ for 90° bend simulations .....	26
Figure 13: Mesh Sensitivity at end of 90° bend using standard k-ε.....	28
Figure 14: Inlet Boundary Condition Compared to Sudo et al (1998) .....	29
Figure 15: Turbulence Model results for outlet of 90° bend.....	30
Figure 16: Wall Model results for outlet of 90° bend .....	31
Figure 17: Comparison of results at outlet of 90° bend .....	32
Figure 18: Velocity Contours from standard k-ε (left) and Sudo et al (1998) (right) at the outlet of the bend .....	33
Figure 19: Velocity vectors from standard k-ε (left) and Sudo et al (1998) (right) for the outlet of the bend. ....	33
Figure 20: Velocity Contour at the end of the bend displaying the additional 4mm and 6mm deflected probe-lines .....	36
Figure 21: Velocity measurements at outlet of bend with measurements taken from 4mm and 6mm using the realizable k-ε turbulence model (4.4m node mesh) .....	37
Figure 22: Flow Distribution for Q=9 LPM using both AFC configurations.....	41
Figure 23: Flow Distribution for all tested total flow rates .....	42

Figure 24: Mesh used in Tee-junction of Manifold .....	44
Figure 25: Wall $y^+$ for Header Assembly simulations .....	45
Figure 26: Flow Distribution for various base mesh sizes using realizable $k-\epsilon$ ...	46
Figure 27: Flow Distribution for Different Inlet Velocity Profiles.....	47
Figure 28: Flow Distribution for various Turbulence Models.....	48
Figure 29: Flow Distribution for various methods .....	49
Figure 30: Flow Distribution with inner diameters modified according to measurements.....	50
Figure 31: Flow Distribution for various turbulence models using modified inner diameters .....	51
Figure 32: Displays the vertical and horizontal planes measured.....	56
Figure 33: Displays seed particle movement between camera frames .....	58
Figure 34: Displays the seed for the J-Nozzle Experiments .....	61
Figure 35: Displays the grid and the number of seed in each grid .....	62
Figure 36: PIV Results - Horizontal Plane Measurements at $Q=1.1\text{LPM}$ and 500Hz capture frequency .....	65
Figure 37: PIV Results - Horizontal Plane Measurements at $Q=1.5\text{LPM}$ and 500Hz capture frequency .....	66
Figure 38: PIV Measurements - Vertical Plane at $Q=1.1\text{LPM}$ 500Hz capture frequency.....	67
Figure 39: PIV Measurements - Vertical Plane at $Q=1.5\text{LPM}$ .....	68
Figure 40: PIV Results - Normalized Horizontal Velocity comparison.....	69

Figure 41: Normalized Vertical Plane Velocity Measurements .....	70
Figure 42: Mesh with 0.193mm base size used for J-nozzle simulations.....	71
Figure 43: Wall $y^+$ for J-Nozzle Simulations ( $Q=1.5\text{LPM}$ ).....	73
Figure 44: Mesh Study- Velocity Field along Horizontal Centreline using realizable $k-\epsilon$ .....	74
Figure 45: Mesh Study - Velocity Field along vertical centreline using realizable $k-\epsilon$ .....	75
Figure 46: Inlet Boundary Condition Test - Horizontal Velocity Field.....	76
Figure 47: Inlet Boundary Condition Test - Vertical Velocity Field.....	77
Figure 48: Turbulence Study - Velocity along Horizontal Plane .....	78
Figure 49: Turbulence Study - Velocity along Vertical Plane.....	79
Figure 50: Velocity Contour of J-Nozzle outlet using realizable $k-\epsilon$ ( $Q=1.5\text{LPM}$ ) .....	80
Figure 51: Horizontal Velocity Profile - Experiment compared to realizable $k-\epsilon$	81
Figure 52: Vertical Velocity Profile - Experiment compared to realizable $k-\epsilon$ ....	82
Figure 53: Centreline Velocity Decay for J-Nozzles ( $Q=1.5\text{LPM}$ ).....	93
Figure 54: Horizontal Velocity Profiles for March 20th Experiment ( $Q=1.5\text{LPM}$ ) .....	94
Figure 55: Vertical Velocity Profile for March 30th Experiment ( $Q=1.5\text{LPM}$ )...	95
Figure 56: Displays velocity profile at $x/D=0$ for $Re=10,000$ ( $Q=4.0\text{LPM}$ ) and a capture frequency of 500Hz.....	96

Figure 57: Radial velocity profiles obtained on 09/05/2017 for Re=10,000 (Q=4.0 LPM).....	97
Figure 58: Radial velocity profiles for Re=25,000 (Q=10.0 LPM), obtained on 09/05/2017 .....	98
Figure 59: Centreline velocity decay of PIV results compared to Literature .....	99
Figure 60: Radial velocity profile from PIV compared to Literature at x/D=1 from the pipe outlet.....	100
Figure 61: Main Channel Tube with eight locations for discharge ports .....	101
Figure 62: Header Manifold with eight discharge ports .....	102
Figure 63: Discharge Port Welded onto main channel .....	103
Figure 64: Main Channel for Assembly with six discharge ports locations .....	104
Figure 65: Manifold with six discharge ports .....	105

## II. List of Tables

Table 1: RMS percent errors relative to measurements by Sudo et al (1998) .....	34
Table 2: Design Values for Header Assembly.....	38
Table 3: Measurements of Discharge Port Inner Diameters .....	54
Table 4: Performance of each model relative to experiment .....	55
Table 5: Repeatability Criteria for Vertical and Horizontal plane measurements (Q=1.5LPM) .....	63
Table 6: Normalized RMS Percent errors for repeatability criteria (Q=1.5LPM) .....	64
Table 7: NRMS Error values for CFD models relative to experiment .....	82

### III. List of Variables

A	Cross-sectional Area (m <sup>2</sup> )
AFC	Alicat Flow Controller
$\beta$	Average velocity ratio in manifold
CANDU	CANadian Deuterium Uranium
CFD	Computational Fluid Dynamics
D	Diameter (m)
ID	Inner Diameter
OD	Outer Diameter (m)
$\delta_{ij}$	Kronecker Delta Function
$\varepsilon$	Turbulent Dissipation Rate (m <sup>2</sup> /s <sup>3</sup> )
F	Non-Dimensionalized Friction Factor (sect 2)
F	Fraction from Uniformity (sect 3)
f	Capture Frequency (Hz)
GCI	Grid Convergence Index
$g_c$	Gravitational Correction Factor (ft/s <sup>2</sup> )
k	Turbulent Kinetic Energy (J/kg or m <sup>2</sup> /s <sup>2</sup> )
k,K	Minor Loss Coefficient
LDV	Laser Doppler Velocimetry
LWR	Light Water Reactor
$\dot{m}$	Mass Flow Rate (kg/s)

NRMS	Normalized Root Mean Square
$p$	Pressure (Pa)
$P, P'$	Non-Dimensionalized Pressures
PJ	Porous Jump
PIV	Particle Image Velocimetry
$\rho$	Density (kg/m <sup>3</sup> )
$\overline{\rho u_i' u_j'}$	Reynolds Stress (Pa)
Q	Volume Flow Rate (m <sup>3</sup> )
Re	Reynolds Number
R	Radius of pipe/tube (m)
RANS	Reynolds Averaged Navier-Stokes
RMS	Root Mean Square
$S_{ij}$	Mean Stress Tensor (1/s)
$\sigma$	Standard Deviation
$\tau_{ij}$	Reynolds Stress Tensor (Pa)
$u$	Velocity (m/s)
U	Time-Averaged Velocity (m/s)
$U_b$	Bulk Fluid Velocity (m/s)
$u'$	Fluctuating Velocity Component (m/s)
$u_\tau$	Friction Velocity (m/s)
$\mu$	Dynamic Viscosity (kg/m s)
$\nu$	Kinematic Viscosity (m <sup>2</sup> /s)

$\nu_T$	Eddy Viscosity (m <sup>2</sup> /s)
V,v	Velocity (m/s)
$\omega$	Specific Dissipation Rate (1/s)
W	Velocity (m/s)
$\Omega_{ij}$	Mean Vorticity Tensor (1/s)
y	Distance from wall (m) (sect 1.2.3)
y	Distance from nozzle centre horizontal (m) (sect 3.3)
y+	Non-dimensional distance from wall
z	Distance from nozzle centre vertical (m)

## **1 INTRODUCTION**

Nuclear reactors convert mass into energy through fission chain reactions. The energy released from fission is primarily from the kinetic energy of the fission products, kinetic energy of the emitted neutrons and emitted gamma rays. Most reactors in the world today are called “Thermal” reactors. This is because they mostly rely on fission induced by thermal neutrons which typically happens with U-235, Pu-239 and Pu-241 due to their fissile nature. In order to keep the fission chain reaction going, thermal reactors require moderators. This is because neutrons created from fission are higher energy or fast. As a result, the moderators needs to slow down fast neutrons to thermal energies to allow for more fission to occur.

A CANDU reactor can be thought of as a cylinder approximately 8 m in diameter and 6 m in length lying on its side with many smaller cylinders inside of it. This cylinder is referred to as the calandria, and the smaller cylinders are known as the calandria tubes. These calandria tubes house the pressure tubes which contain the fuel bundles and the heavy water coolant. This can be visualized in Figure 1.



Figure 1: Displays CANDU reactor calandria and other components from [1]

## 1.1 CANDU Moderator

The moderator of a CANDU, is a very large body of heavy water kept at atmospheric pressure. The moderator thermalizes fast neutrons from fission into thermal neutrons to maintain the fission chain reaction. The main moderator heat source is thermalization of neutrons, though gamma rays from decaying fission products provide additional energy. Hence, a volumetric heat source is distributed in the calandria vessel. Being constantly heated the moderator requires its own cooling system separate from the primary heat transport system to remove this heat.

The moderator also acts as an emergency heat sink for the fuel in severe accident scenarios. During these postulated accidents the pressure tube could balloon or

sag into contact with the calandria tube. This would allow for the heat from the fuel to be conducted into the moderator. However, depending upon the local moderator subcooling (how far below the local temperature is below saturation temperature), critical heat flux (CHF) may occur. This would result in a rapid ascent in temperature of the calandria tube and could result in the channel failing - see [2] and [3] for a comprehensive review on moderator flow studies.

The Moderator Test Facility as displayed in Figure 2 was built at McMaster University to aid the validation of computer codes/models. Both flow and temperature fields are being measured using the optical Laser Doppler Velocimetry (LDV) system and a set of thermocouples respectively. This facility consists of three main components, Header Assemblies, Flow Controllers and the Vessel as displayed in Figure 2. The flow enters the tank through 22 J-nozzles fed from 3 header assemblies. The flow through each of these header assemblies is controlled using 2 flow controllers. The vessel contains 52 heated rods and 68 unheated rods and flow exits through two outlets on the bottom of the tank as seen in Figure 2. This particular study will focus on determining the inlet flow conditions of this facility and as such will focus on the Header Assemblies.

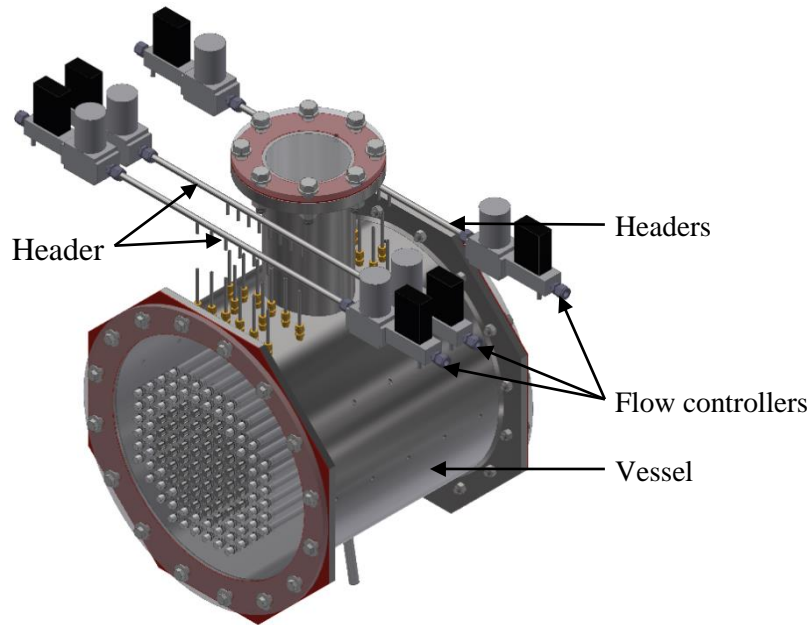


Figure 2: Isometric of Moderator Test Facility

A typical Header Assembly for this test facility can be seen in Figure 3. The assembly contains a dividing manifold with 8 J-nozzles connected by flex lines (plastic tubes) to the header. It should be noted that for the actual facility that there exist two assemblies as shown in Figure 3 and one additional assembly that contains only 6 J-nozzles.

To properly characterize the inlet flow conditions into the moderator vessel, three distinct flow phenomena need to be investigated: turbulent bent pipe flow, turbulent free jets and dividing manifold flow conditions. The end goal is to determine which turbulence model will perform best by comparing CFD results to experiments performed in the course of the present study and those found in

literature. This will potentially allow for the optimal turbulence model for all three flows to be determined. This is intended to aid subsequent CFD simulations of the moderator facility.

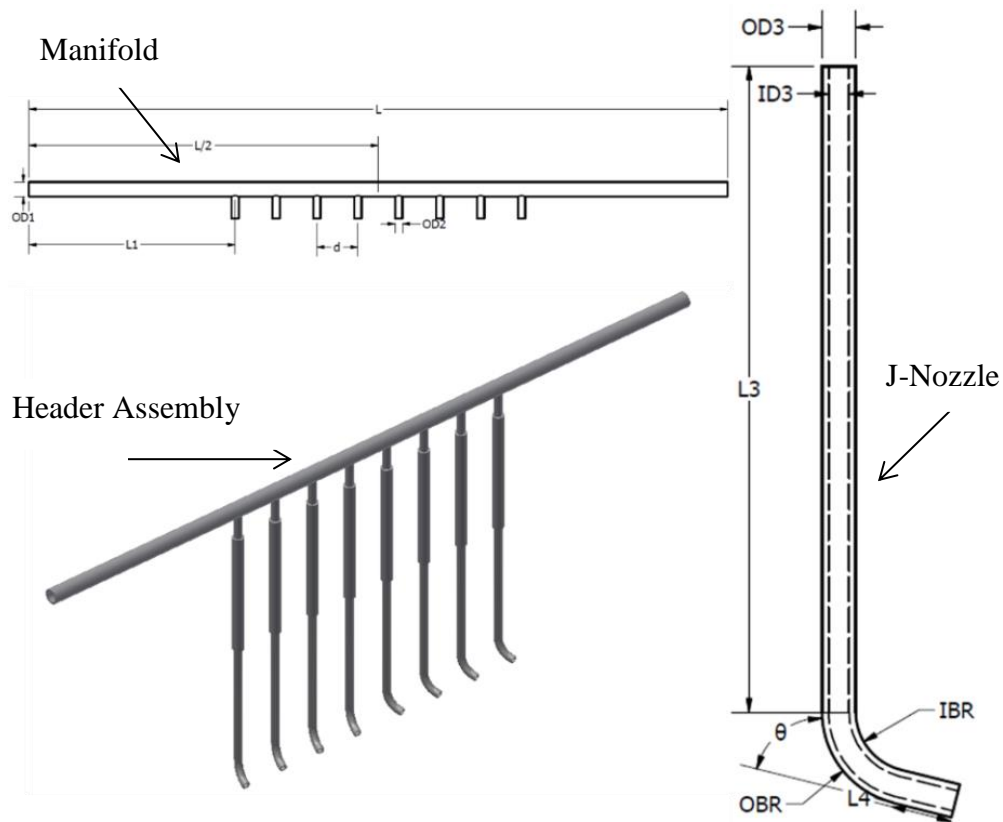


Figure 3: Header Assembly for the Moderator Test Facility (bottom left), manifold (top) and J-Nozzle (right)

Section 1.2 introduces the concepts that aid the understanding computational fluid dynamics and turbulence modelling.

## 1.2 Computational Fluid Dynamics

Computational Fluid Dynamics (CFD) is the numerical method by which the Navier-Stokes equations for mass, momentum and energy are solved. The method typically employed is the finite volume method due to its conservative nature as outlined below.

### 1.2.1 Finite Volume Method

The finite volume method is designed to split a domain into several control volumes. The intent of this method is to ensure that the conservation laws are strictly upheld at all times. This means that over a control volume the inlet and outlet fluxes of a given quantity (such as mass or momentum) must be equal by the definition of the method. This is to ensure that the numerical solution obtained is physical. Over each of these control volumes, every quantity is averaged resulting in one value for every property in that control volume. For example this would mean that there is only one velocity and one pressure value for the control volume P on Figure 5. This allows for the discretization of the Navier-Stokes equations and numerical solution. To illustrate this, consider a domain split into three points, W, P and E as shown in Figure 4.

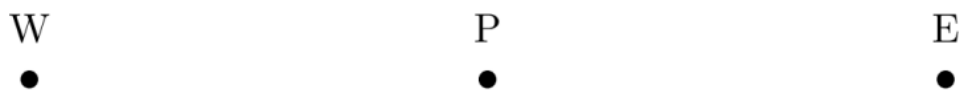


Figure 4: Displays discretization of domain

To implement the Finite Volume method, we must consider each of these points to be a control volume, which can be visualized in Figure 5. Each of these control volumes have all of their quantities averaged over their domain. This means that in every control volume there is only 1 velocity, temperature, density and so on. It should be noted that each control volume face as labelled w and e for control volume P on Figure 5 plays an important role when handling gradients.

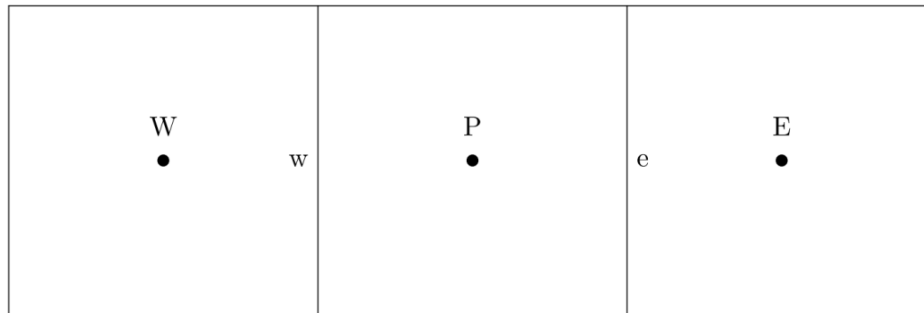


Figure 5: Displays Control Volumes around points W, E and P

By generating an equation for each control volume we can obtain a series of linear algebraic equations which can then be constructed into a matrix and solved. For more discussion and information on how to discretize and solve the Navier-Stokes equations using the Finite Volume Method the reader is referred to [4].

### 1.2.2 Turbulence Modelling

Turbulence is the phenomena by which flows above a certain Reynolds number (~4000) begin to exhibit random fluctuations in flow parameters such as velocity.

To resolve this, the Navier-Stokes equations must be solved to very fine time and length scales. Unfortunately, this is prohibitively expensive for most engineering applications. The primary methods of dealing with turbulence numerically are Direct Numerical Simulation (DNS), Large Eddy Simulation (LES) and Reynolds Averaged Navier-Stokes Equations (RANS). The most popular method is RANS and it will be examined below in some detail.

### 1.2.2.1 The Reynolds Decomposition and RANS

As a potential solution to the turbulence problem the velocity in the Navier-Stokes was split into a fluctuating ( $u'$ ) and a mean ( $U$ ) component as shown in equation (1).

$$u = u' + U \quad (1)$$

By definition, the time average of the mean term would simply be the velocity and the fluctuating term would vanish.

$$\overline{u'} = 0 \quad (2)$$

$$\overline{u} = \overline{U} = U \quad (3)$$

Starting with the Navier-Stokes in a slightly modified (conservative form of non-compressible flow) form (4), we can apply Reynolds Decomposition and time averaging (equations (2) and (3) ) to obtain equation (5) for each direction, i, j and k.

$$\rho \frac{\partial u_i}{\partial t} + \rho \frac{\partial (u_i u_j)}{\partial x_j} = -\frac{\partial P}{\partial x_j} + \frac{\partial}{\partial x_j} (2\mu S_{ji}) \quad (4)$$

$$\rho \frac{\partial U_i}{\partial t} + \rho \frac{\partial}{\partial x_j} (U_j U_i + \overline{u'_i u'_j}) = -\frac{\partial P}{\partial x_i} + \frac{\partial}{\partial x_j} (2\mu S_{ji}) \quad (5)$$

$$\rho \frac{\partial U_i}{\partial t} + \rho U_j \frac{\partial U_i}{\partial x_j} = -\frac{\partial P}{\partial x_i} + \frac{\partial}{\partial x_j} (2\mu S_{ji} - \overline{\rho u'_i u'_j}) \quad (6)$$

Equation (6) is obtained from equation (5) and is known as the Reynolds Averaged Navier-Stokes equation, or RANS for short. In developing this equation an additional set of 6 unknowns,  $\overline{\rho u'_i u'_j}$  known as the Reynolds stresses are obtained from the time averaging process and the Reynolds decomposition. These particular terms are problematic as there is no known explicit relation for them. If we attempt to write a transport equation for each Reynolds stress we would obtain 6 additional equations, but would gain 22 additional unknowns with terms such as  $\overline{\rho u'_i u'_j u'_k}$ . This is known as the closure problem and various turbulence models seek to obtain expressions for the six turbulent stresses in terms of the mean flow field variables to solve equation (6).

There have been many attempts to close this system of equations with one of the earliest attempts being Prandtl's Mixing Length model. Currently the most popular methods used to close this system of equations are the two-equation turbulence models. These models are the most popular as they are complete, which means that no prior information is needed about the turbulent structures to

predict flow properties [5]. They are also popular as they have been validated for a wide variety of flows and have been used for over 30 years.

### 1.2.2.2 Two-Equation Models

Two-equation turbulence models are based on the Boussinesq approximation. This approximation states that the Reynolds stress can be related to the mean strain of the flow, the eddy viscosity of the flow and the turbulent kinetic energy, it is shown below in equation (7) [5]. It must be noted that the eddy viscosity relation is determined by dimensional analysis and it is not necessarily physically true.

$$-\rho \overline{u'_i u'_j} = 2\nu_T S_{ij} - \frac{2}{3}k\delta_{ij} \quad (7)$$

As seen in equation (7), the turbulent kinetic energy of the flow is important in determining the Reynolds stresses. As a result, most two-equation turbulence models make use of the turbulent kinetic energy  $k$ , and one other variable such as the turbulent dissipation rate  $\varepsilon$ . Popular turbulence models used regularly throughout this report are examined in subsequent sections.

### 1.2.2.3 Standard k-ε Model

This model is based upon two properties of the flow. Turbulent kinetic energy  $k$  and the turbulent dissipation rate  $\varepsilon$  whose transport equations are given by equations (8) and (9) below [5]:

$$\frac{\partial k}{\partial t} + U_j \frac{\partial k}{\partial x_j} = \tau_{ij} \frac{\partial U_i}{\partial x_j} - \varepsilon + \frac{\partial}{\partial x_j} \left[ \left( \nu + \frac{\nu_T}{\sigma_K} \right) \frac{\partial k}{\partial x_j} \right] \quad (8)$$

$$\frac{\partial \varepsilon}{\partial t} + U_j \frac{\partial \varepsilon}{\partial x_j} = C_{\varepsilon 1} \frac{\varepsilon}{k} \tau_{ij} \frac{\partial U_i}{\partial x_j} - \frac{C_{\varepsilon 2} \varepsilon^2}{k} + \frac{\partial}{\partial x_j} \left[ \left( \nu + \frac{\nu_T}{\sigma_\varepsilon} \right) \frac{\partial \varepsilon}{\partial x_j} \right] \quad (9)$$

The goal of this model is to use these two flow properties to back out a relation for the eddy viscosity which can then be used to find the Reynolds stresses needed for the mean momentum conservation equation(6). The method for obtaining the relation between  $k$ ,  $\varepsilon$  and  $\nu_T$  is dimensional analysis. For the k-ε turbulence model, this can be found to be equation (10) where  $C_\mu$  is a constant [5].

$$\nu_T = C_\mu \frac{k^2}{\varepsilon} \quad (10)$$

### 1.2.2.4 Realizable k-ε Model

The main difference between this model and the standard k-ε model is the  $C_\mu$  constant in equation (10). For this model it is not constant but depends on flow parameters. The reason for this change arises when flows exhibit high amounts of shear stress. By examining the Bousinesq approximation in equation (7) if the

mean stress is very high and  $C_\mu$  is a constant then negative normal Reynolds stresses can be obtained. This is not physical and needed to be addressed.

To combat this issue the  $C_\mu$  term in (10) is modified to no longer be a constant, but to be a function of  $k, \varepsilon, S_{ij}$  and  $\Omega_{ij}$  (the mean vorticity) [6]. This model is called realizable as a result of now making the relation physically “realizable” as the normal Reynolds stress will not become negative. These modifications can be seen below as equations (11) and (12) from [6]. For more detail with regards to this model see [6].

$$C_\mu = \frac{1}{A_o + A_s U(*) \frac{k}{\varepsilon}} \quad (11)$$

$$U(*) = \sqrt{S_{ij}S_{ij} + \widetilde{\Omega}_{ij}\widetilde{\Omega}_{ij}} \quad (12)$$

#### 1.2.2.5 k- $\omega$ Model

More options exist other than the k- $\varepsilon$  models. Another popular choice is the k- $\omega$  models. This model uses the rate of dissipation  $\omega$  for its second transport variable instead of  $\varepsilon$ . This term has units of 1/s and has been referred to as the rate of dissipation of turbulent kinetic energy in a unit volume and time [5]. As a result, the turbulent viscosity follows a different relation seen in equation (15). The equations associated with this model can be seen below as equations (13)-(15) below [5]:

$$\frac{\partial k}{\partial t} + U_j \frac{\partial k}{\partial x_j} = \tau_{ij} \frac{\partial U_i}{\partial x_j} - \beta^* k \omega + \frac{\partial}{\partial x_j} \left[ \left( \nu + \sigma^* \frac{k}{\omega} \right) \frac{\partial k}{\partial x_j} \right] \quad (13)$$

$$\begin{aligned} \frac{\partial \omega}{\partial t} + U_j \frac{\partial \omega}{\partial x_j} &= \frac{\alpha \omega}{k} \tau_{ij} \frac{\partial U_i}{\partial x_j} - \beta \omega^2 + \frac{\sigma_d}{\omega} \frac{\partial k}{\partial x_j} \frac{\partial \omega}{\partial x_j} \\ &+ \frac{\partial}{\partial x_j} \left[ \left( \nu + \sigma \frac{k}{\omega} \right) \frac{\partial \omega}{\partial x_j} \right] \end{aligned} \quad (14)$$

$$\nu_T = \frac{k}{\omega} \quad (15)$$

This model is much more accurate in resolving the boundary layer relative to the k-ε and some other models [5]. In an attempt to produce even better models it has even been combined with k-ε models to produce the k-ω SST model. This model essentially uses k-ω to resolve the boundary layer for wall bounded flows and gradually transitions to the k-ε model to resolve the far field flows [7].

For more details regarding turbulence and its modelling, the reader is referred to [5], [6], [8], and [9].

### 1.2.3 Wall Modelling

Flow near a solid surface requires a different treatment in order to resolve the boundary layer correctly and reach the physically correct behavior of the solved

turbulence characteristics, e.g.  $k$ ,  $\epsilon$  and  $\omega$ . Near the wall fluid is slowed down due to the no-slip condition. This means that very close to the wall viscous effects dominant creating a viscous sublayer near the wall. The further out into the main flow the more convective forces begin to dominant for high Reynolds number flows. A non-dimensional distance called  $y^+$  indicates where in the boundary layer a given point is.

$$y^+ = \frac{u_\tau y}{\nu} \quad (16)$$

The high  $y^+$  wall models are valid for  $y^+$  values of 20-100 and employs wall functions to accurately account for the effects of the wall. This is based upon the Law of the Wall shown in equation (17).

$$\frac{U}{u_\tau} = \frac{1}{\kappa} \ln\left(\frac{u_\tau y}{\nu}\right) + C \quad (17)$$

Low  $y^+$  treatments are valid for meshes with their first  $y^+$  values of 5 or lower and as such require much finer grids near the wall. Wall functions are not used for this model as it resolves the entire boundary layer assuming the mesh is fine enough [7].

There exist an all  $y^+$  treatment in commercial CFD codes such as STAR-CCM+. This treatment would attempt to act like the high  $y^+$  wall model for coarse grids and the low  $y^+$  model for finer grids [7].

For more details into wall modelling see [5], [7] and [9].

## **2 LITERATURE REVIEW**

The following review was focused on three flow areas: flow through manifolds, bends and turbulent round jets. These three areas were chosen as they all occur in the header assembly and are identified in Figure 6.

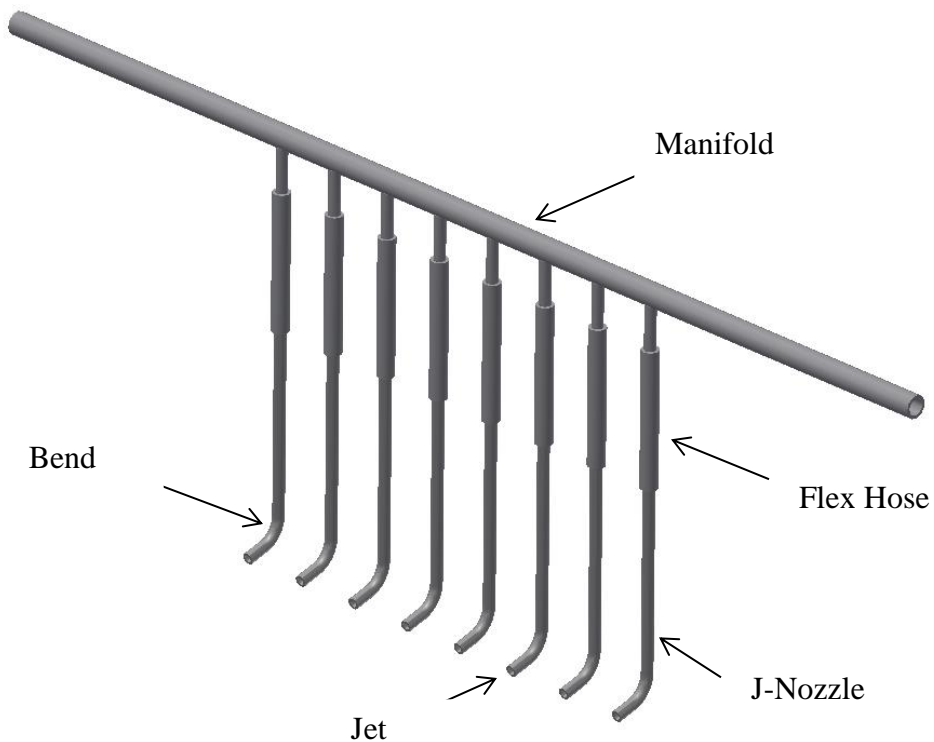


Figure 6: Isometric of Header Assembly

## 2.1 Manifolds

A manifold consists of a main channel with multiple smaller tubes attached with the intention to distribute the flow as can be seen in Figure 7. The typically smaller tubes are referred to as ports with the area between them referred to as branches see Figure 7. A dividing manifold is when the flow in the manifold goes from the main channel into the smaller tubes otherwise known as discharge ports for this case To determine flow distributions one may employ simulations (CFD), analytic calculations, discrete models and experimentation.

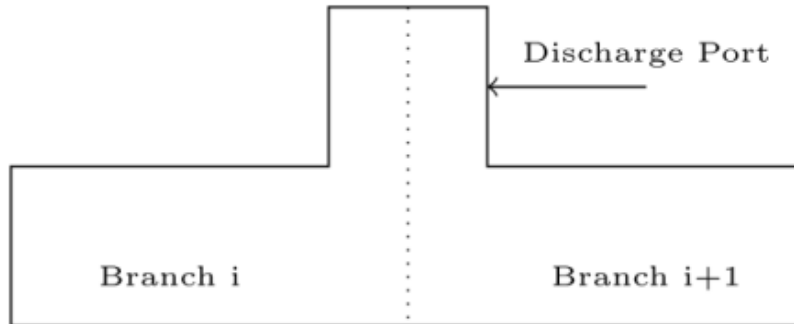


Figure 7: Displays Manifold Branches and Discharge Ports

The flow distribution of a dividing manifold is governed by the friction, momentum forces and geometry effects [10]. These forces have a competing effect on the pressure distribution in the main channel of the manifold with friction lowering the pressure and the momentum forces acting to increase the channel pressure at the discharge ports [10]. This effect can clearly be seen in Figure 8 below. The discharge angle is the angle at which fluid enters the discharge port [10]. A discharge angle of 90-degrees would correspond to no axial velocity in the discharge port and thus a maximum pressure rise in the main channel [10] which would be given by equation (18). Since this is not always the case a loss coefficient  $k$  is introduced to obtain the real pressure rise ( $k < 1$ ) - equation (19).

$$p_2 - p_1 = \frac{\rho(V_1^2 - V_2^2)}{g_c} \quad (18)$$

$$p_2 - p_1 = \rho k \frac{V_1^2 - V_2^2}{g_c} \quad (19)$$

The discrete model of Acrivos et al [10] employs equations (20) to (22) in order to sequentially solve for the non-dimensional velocities and pressures for branches in the main channel. To perform a calculation, one would first calculate the pressure at the end of the branch using (20) to account for frictional effects. After obtaining the pressure just before the discharge port, the bulk fluid velocity is calculated using (21). Now that the velocity in the next branch is known equation (22) is used to determine the pressure rise and thus the pressure on the other side of the discharge port. This process is repeated until all of the branches have been solved <sup>1</sup>.

$$P'_i - P_i^o = -F_i U_i^2 \Delta y \quad (20)$$

$$U_{i+1} = \frac{1}{1 + \frac{(\Delta y)^2}{2}} \left[ U_i - \sqrt{\frac{(\Delta y)^4}{4} U_i^2 + 2(\Delta y)^2 \left( 1 + \frac{(\Delta y)^2}{2} \right) P'_i} \right] \quad (21)$$

$$P_{i+1}^o - P'_i = \frac{1}{2} (U_i^2 - U_{i+1}^2) \quad (22)$$

---

<sup>1</sup> 1 is for upstream of a discharge port and 2 is for downstream of a discharge port

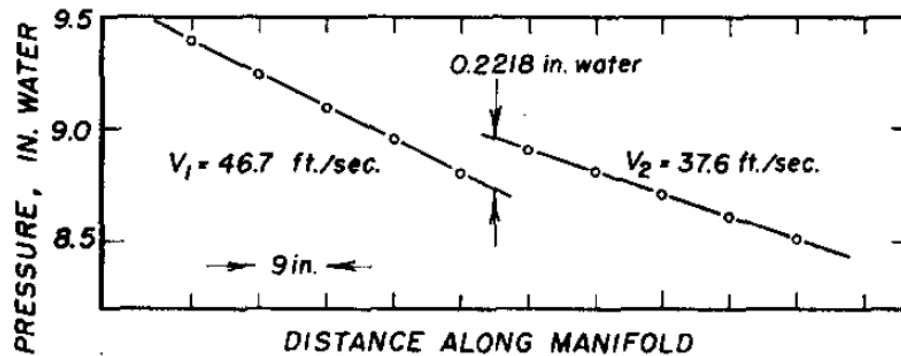


Figure 8: Displays the pressure increase in the main channel of a manifold after a discharge port from [10]

A study was performed by Chen and Sparrow [11] in which a 39 outlet manifold was examined by experiment and CFD. Using air as their working fluid and performing a comprehensive mesh study, Chen and Sparrow [11] showed that the flow distribution, pressure variation and the discharge angle were captured best by using the realizable  $k-\epsilon$  turbulence model.

Tomor and Kristof [12] performed a study in which they compared predictions by discrete model to results obtained from CFD and experiment for a dividing manifold geometry. They demonstrated that their discrete model was able to predict the flow rate out of each discharge port within uncertainty of experiment with results comparable to CFD for Reynolds numbers of 13200 to 39200. The model of Tomor and Kristof [12] differs from that of Acrivos et al [10] as it relies on tables of constants for given geometries (i.e. fixed area ratios, length ratios etc).

In addition to discrete models, a lot of effort has been put into analytic models of manifolds, some studies include [13-16]. These analytic methods are all based on solving equation (23) below [14].

$$\frac{1}{\rho} \frac{dP}{dx} + \frac{f}{2D} W^2 + \frac{2 - \beta}{2} \frac{dW^2}{dx} = 0 \quad (23)$$

It should be noted that the analytical solution to this equation would be for the case in which the manifold has a continuous discharge port along its length, which can also be thought of as the distance between ports of zero. This equation is based upon conservation of momentum with the terms from left to right representing the change in pressure, frictional losses and pressure recovery after a discharge port. Note that the maximum pressure recovery is obtained with  $\beta=0$ , as this would represent fluid leaving the main channel at  $90^\circ$  angles. Even though the case of continuous discharge ports may not occur frequently, analytical solutions are still very useful as they are the limiting case for discrete solutions. They can also be applied to real manifolds in the event that they have many discharge port with small distance between them.

When examining these studies, it can be determined that discrete models and CFD simulations can be very accurate when predicting manifold parameters such as the

mass flow distribution. When using CFD, the realizable  $k-\varepsilon$  turbulence model should be chosen as it has been prove to provide the best results.

## 2.2 Flow in bends

Flow in curved tubes has been extensively covered by both experiment and simulation through CFD as shown by [17-21].

Sudo et al [17] examined turbulent flow in a 90-degree circular-sectioned bend using hot-wire anemometry. They used air as a working fluid with bend radius of curvature of four times the tube radius ( $4.0R$ ), Reynolds number of 60,000 and long entry length of 100 diameters to ensure a fully-developed flow at the bend entrance. A series of contours were reported which illustrate the flow structure before the bend, in the bend and after the bend. The general trend is that most of the momentum is concentrated in the inside of the bend, which increases the velocity in that. Then as the fluid reaches the end of the bend, the higher velocity region moves to the outside of the tube. This experiment is analyzed in greater detail in section 3.1.

Validation of CFD against various flow conditions using experimental data has been done extensively, flow in curved tubes is no exception as reported by [18] and [20]. Kim et al [18] performed a CFD investigation into bent pipe flow by attempting to validate their results and choice of turbulence model against the data

of Sudo et al [17]. By defining a “hit” as a point that has a velocity that is within  $\pm 10\%$  of the experimentally obtained values for various sections of the bend. Kim et al [18] found that the realizable  $k-\epsilon$  and  $k-\omega$  SST turbulence models had the highest number of hits while the RNG  $k-\epsilon$  model was found to have the lowest standard deviation relative to experiment.

### 2.3 Turbulent Round Jets

The structure of turbulent flow in round jets has been investigated both numerically and experimentally over the years in studies - see e.g. [22-26].

Boguslawski and Popiel [22] experimentally studied the flow structure of a turbulent round jet in the near-nozzle region. Using a pipe of 50 diameters in length to achieve fully developed flow, measurements were made using hot-wire anemometry. Using these conditions, Boguslawski and Popiel [22] measured the radial and axial distributions of the velocity in addition to turbulent intensities and kinetic energy.

G. Xu and R.A. Antonia [23] investigated how the inlet velocity profile impacts turbulent round jets. To do this, they compared a top-hat velocity profile (smooth contraction) to a fully-developed profile (pipe jet) and measured the velocity fields in the jet using hot-wire anemometry. They found that different inlet conditions yielded different turbulent structures with the pipe jet resulting in longer wavelength structures relative to the smooth contraction in both the near

and far field. This was thought to be a result of the pipe jet having a larger initial shear layer thickness.

As previously mentioned, RANS is a popular choice for CFD simulations. Unfortunately, as illustrated by Smith et al [26], two-equation models used in RANS cannot model large scale turbulent structures which lead to numerical results which contradict experiment for jet propagation. Geogiadis et al [25] performed a turbulence modelling study by comparing several modified two-equation models thought to better model the mixing of jets than unmodified two-equation models. The main issues with the unmodified models was that the prediction of the length required for the centreline velocity to decay were too long relative to experiment which means that the dissipation is being underestimated. Although Geogiadis et al [25] saw some improvement in terms of mean flow predictions, the turbulent kinetic energy predictions offered no improvement from those made by standard models.

### **3 RESULTS**

#### **3.1 Flow through Bent Circular Tubes**

As the J-nozzles in the header assembly contain  $76^\circ$  bends, flow in curved tubes with similar bends are first investigated. This was done by performing a CFD investigation into flow through  $90^\circ$  bends as there have been experiments done to provide data for validation exercises. The experiment chosen was that performed by Sudo et al [17] who examined turbulent flow through a  $90^\circ$  bend.

### 3.1.1 Experimental Setup of Sudo et al (1998)

The experiment was performed using air with steady-state conditions for turbulent flow through a circular-sectioned elbow ( $90^\circ$  bend). The piping used had an inner diameter of 104mm, the radius of curvature of the bend as 208mm and Reynolds number was set at 60,000 [17]. To ensure fully-developed flow the inlet velocity field of air at  $8.7\text{m/s}$ <sup>2</sup> was given 100 pipe diameters of entry length, this can be seen in their experimental setup presented in Figure 9

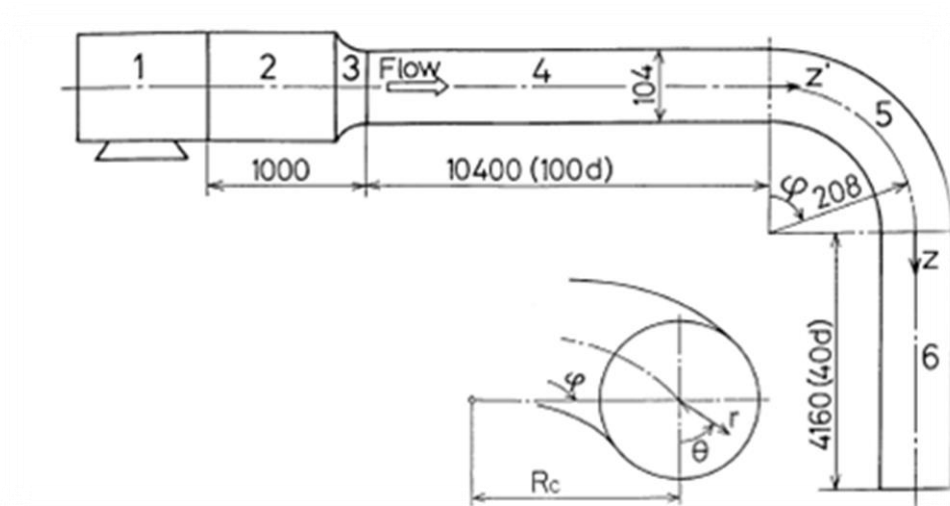


Figure 9: Sudo et al (1998) Experimental Setup [17]

The measurement grid of the hot-wires used by Sudo et al (1998) can be seen on Figure 10. It can be noted that the grid coarsens near the inner and outer regions of the pipe. This may be of importance in analyzing the impact of positional uncertainties as they were not recorded in the paper itself. An estimate for the size

<sup>2</sup> The bulk fluid velocity  $U_b$  of 8.7m/s is the normalizing factor for all subsequent plots in this section

of the measurement volume for points near the tube walls can be made by noting that there are 18 circumferential measurements in Figure 10. By calculating the circumference and dividing by 18, the length of each wedge can be found to be 9.08mm.

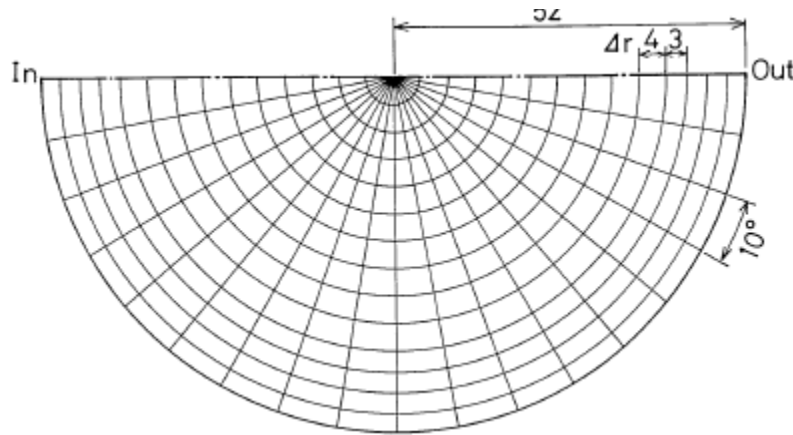


Figure 10: Sudo et al (1998) Measurement Grid [17]

### 3.1.2 CFD Setup for the Bend

The geometry was created exactly as described by Sudo et al (1998) [17] to ensure that the experiment was being modelled properly with one exception being that only half of the geometry was created. This was done to take advantage of symmetry so that a smaller number of nodes could be used, which can be seen in the mesh on Figure 11. The grid was designed to be of an O-grid shape using the "directed meshing" tool in STAR-CCM+ which allowed for the pattern to be swept through the bend as seen in Figure 11. The number of axial divisions was

fixed at 2000 as changing this value to 4000 did not show any significant difference in the results obtained.

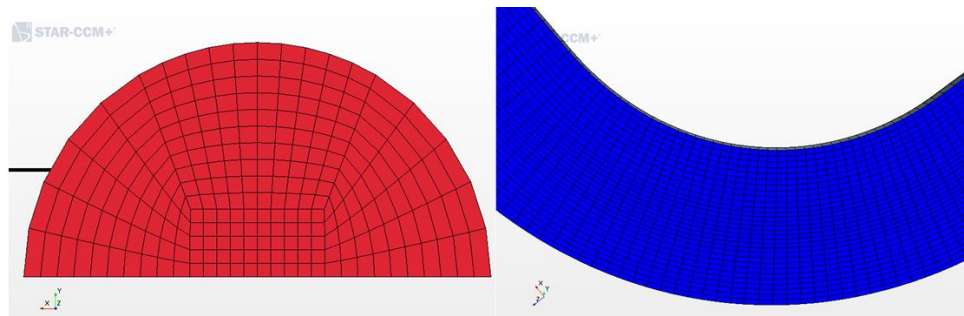


Figure 11: Grid for the 90° bend

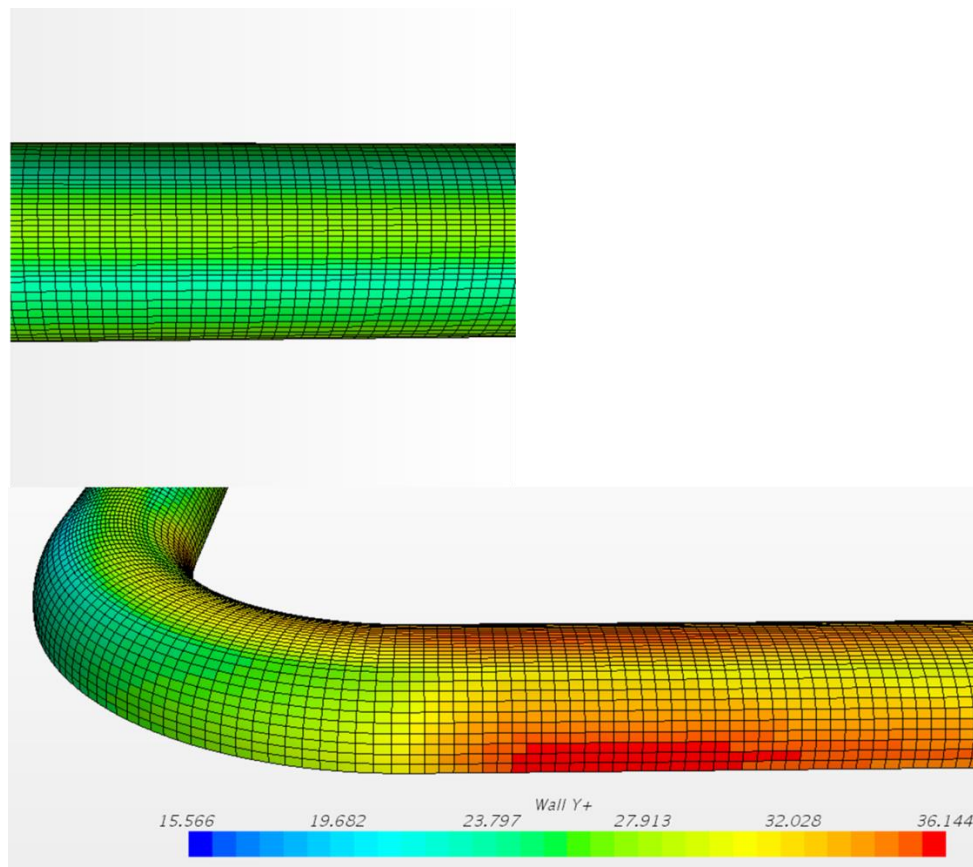


Figure 12: Wall Y+ for 90° bend simulations

The simulations were ran until convergence was achieved. For simulations in this section and subsequent simulations, convergence was determined when the residuals in the simulation were sufficiently low with values at or lower than  $10^{-4}$ . Another indicator was the change in relevant parameters (velocity, mass flow rate, etc) between iterations. When simulations would not converge to residuals of  $10^{-4}$  or less, the simulations were ran until the change in those relevant parameters was less than 1/1000 of a percent.

### 3.1.2.1 Mesh Study

As it was found that 2000 axial divisions was sufficient, the number of cells in the cross-section were varied to test the impact of the grid on the solution. This was to ensure that the numerical solution was mesh insensitive before performing other modelling tests.

CFD results were obtained along the diameter of the tube at the outlet of the bend. These velocities can be seen in Figure 13. In Figure 13 it is seen that the solution is very sensitive to the grid size in the  $r/R < -0.3$  region. This is likely due to a pressure gradient which gets resolved differently as the number of cells in this region is varied.

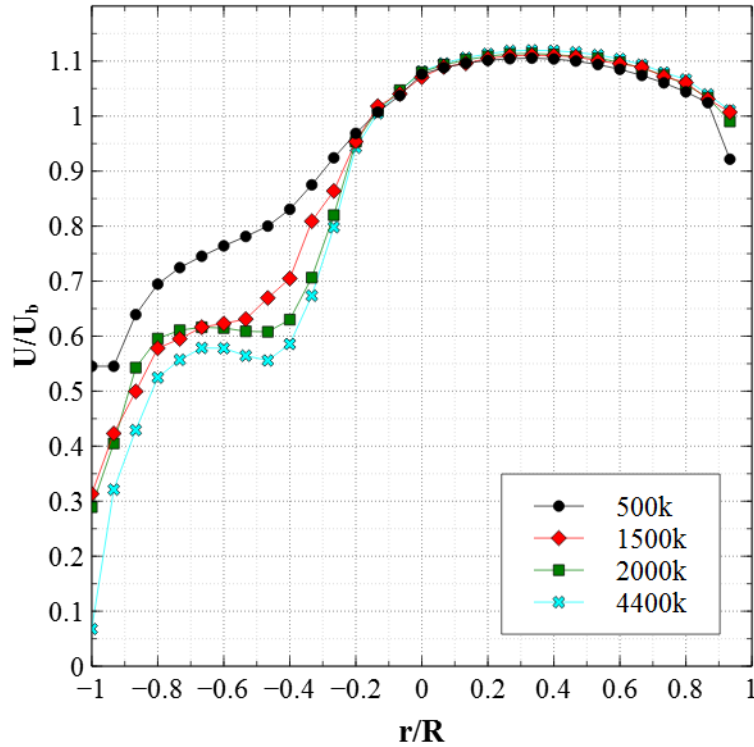


Figure 13: Mesh Sensitivity at end of 90° bend using standard k-ε

To ensure that the solution is sufficiently converged, the Grid Convergence Index (GCI) was calculated for the fine grid solution using equation (24) below [27].<sup>3</sup>

$$GCI = \frac{3|\epsilon|}{(r^p - 1)} \quad (24)$$

The GCI of the fine grid solution was found to be 3.06% in refining from 2000k to 4400k. This indicates that the solution is fairly grid independent in spite of the troublesome  $r/R < -0.3$  region. Qualitatively there are only small deviations in velocity profile over the range of 1500k to 4400k nodes.

<sup>3</sup>  $\epsilon$  is the percent difference between grid,  $r$  is the grid ratio (2 would be doubling) and  $p$  is the order of the numerical method i.e 2<sup>nd</sup> order differencing.

### 3.1.2.2 Inlet Boundary Condition

Sudo et al (1998) recorded an inlet condition consistent with Fully-Developed flow at a position 1 pipe diameter upstream from the inlet to the bend. To ensure meaningful CFD results, this inlet condition needed to be matched. Figure 14 shows the fully-developed velocity profile that CFD predicts for two different turbulence models compared to experiment. It can be seen that there is a satisfactory agreement between experiment and simulation which means that the CFD simulations do indeed have fully-developed turbulent flow heading into the pipe-bend.

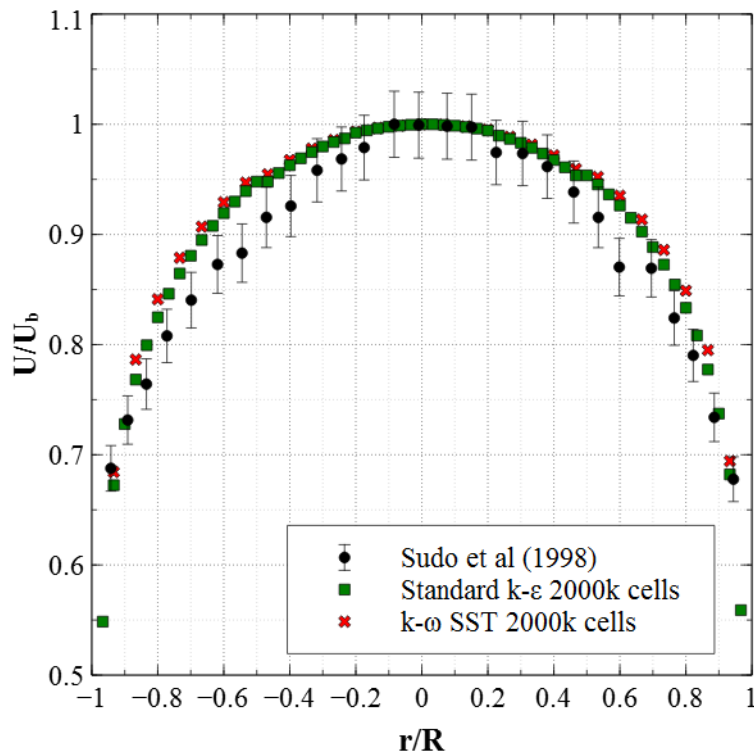


Figure 14: Inlet Boundary Condition Compared to Sudo et al (1998)

### 3.1.2.3 Numerical Results

In order to determine which turbulence model will give the best results for the case of the bent pipe flow, standard k- $\epsilon$ , realizable k- $\epsilon$ , k- $\omega$  SST and Spalart-Allmaras were used with the 2000k cell mesh. The result of these simulations can be seen in Figure 15 below.

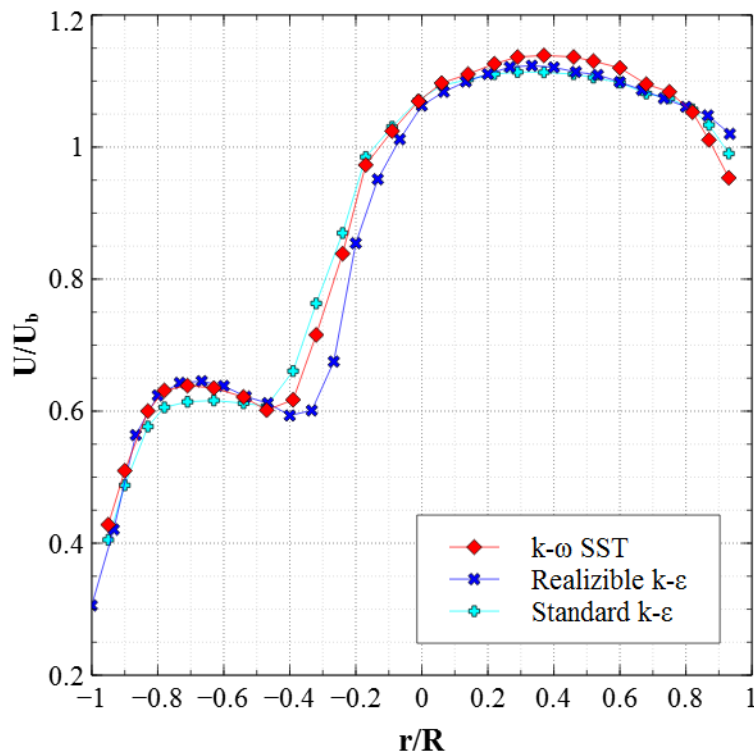


Figure 15: Turbulence Model results for outlet of 90° bend

### 3.1.2.4 Wall Model Testing

The choice of wall-model can also have an impact upon the solution as the low  $y^+$  models resolves the viscous sub-layer whereas the high  $y^+$  ones start in the log-layer. The result of these two models and the all  $y^+$  model can be seen in Figure

16. It can be noted that the high and all  $y^+$  models yield the same results, whereas the low  $y^+$  model does have some impact on the solution. This however may have been a result of the grid refinement required to adequately use the low  $y^+$  model as well.

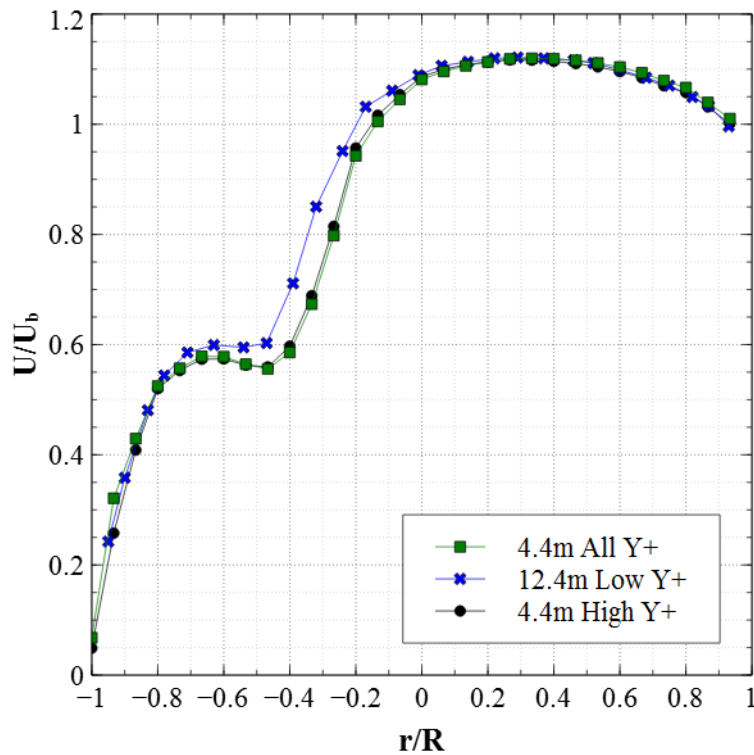


Figure 16: Wall Model results for outlet of 90° bend<sup>4</sup>

### 3.1.3 Comparison to Experiment and Separate Numerical Study

Figure 17 shows the comparison of these CFD simulations with the experiments by Sudo et al [17]. Numerical results reported by Kim et al [18] are also presented for the same experimental conditions. It should be noted that the results displayed

---

<sup>4</sup> Note: a different grid was used for the low  $y^+$  wall model results

from Kim et al [18] where obtained using the standard k- $\epsilon$  turbulence model. It can be seen that there is a significant difference between simulation and experiment in the  $r/R < -0.3$  region (near the inner wall of the bend). This was also found by Kim et al [18] who attributed this difference to the presence of an adverse pressure gradient generating swirl in the pipe.

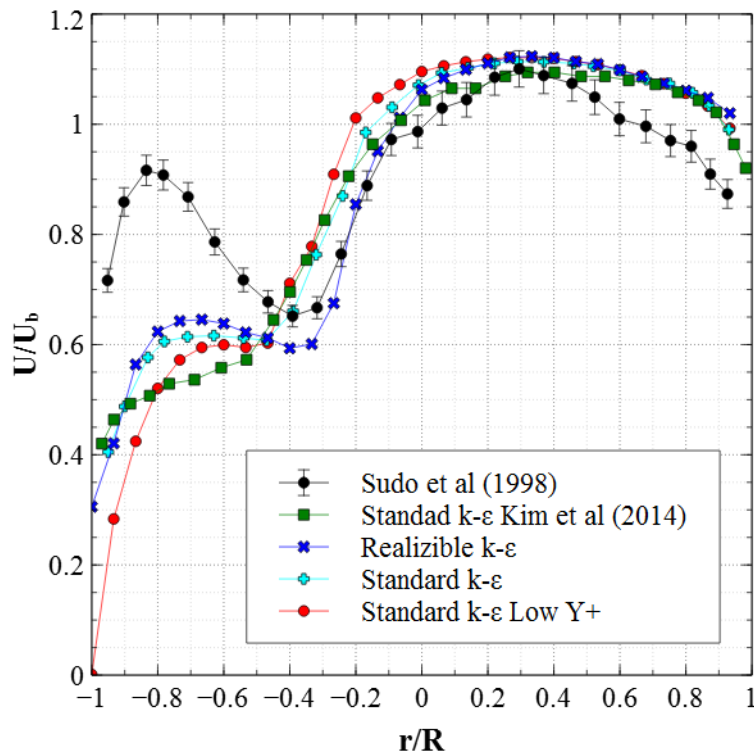


Figure 17: Comparison of results at outlet of 90° bend

A comparison of the velocity contours at the outlet cross-section of the bend is presented in Figure 18. While it is hard to get a quantitative measure of how well the simulation is capturing the velocity profile by looking at a contour, it is

evident that both CFD and experiment show a high velocity gradient in the inner region of the bend ( $r/R < -0.3$ ) - see Figure 18.

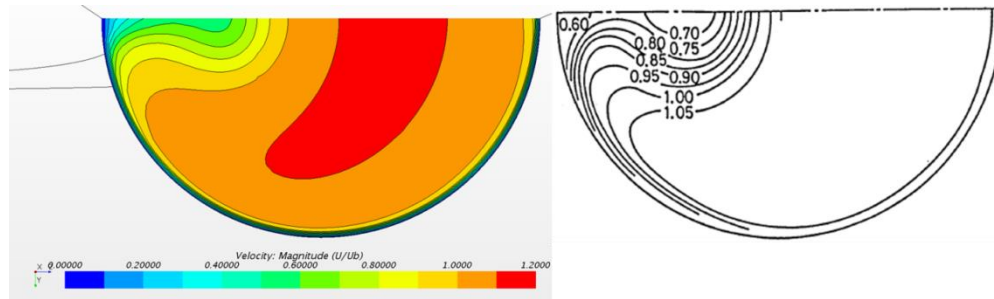


Figure 18: Velocity Contours from standard  $k-\epsilon$  (left) and Sudo et al (1998) (right) at the outlet of the bend

The transverse vectors were plotted alongside those seen in experiment at the end of the bend in Figure 19 below. As mentioned before, it is hard to get a quantitative measure of how well STAR-CCM+ is actually performing using this kind of comparisons, but it can be seen in Figure 19 that STAR-CCM+ is predicting the existence of a vortex in the same region as measured in experiment. This gives some added confidence that the CFD simulation results are not inherently flawed and hold some merit.

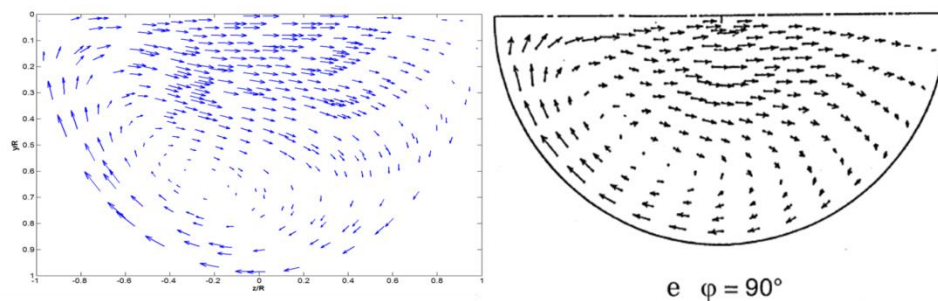


Figure 19: Velocity vectors from standard  $k-\epsilon$  (left) and Sudo et al (1998) (right) for the outlet of the bend.

To get a quantitative measure as to how well each model performs the RMS error of each model was calculated relative to experiment. These values were normalized by the bulk fluid velocity and converted to a percent error - see equations (25) and (26). Results are shown in Table 1 and it can be seen that the realizable k- $\epsilon$  turbulence model shows lowest RMS percent error. It should be noted that the improvement that realizable k- $\epsilon$  provides over the other 2-equation models is marginal.

$$\sigma = \sqrt{\frac{\sum_{i=1}^N (v_{CFD} - v_{EXP})^2}{N}} \quad (25)$$

$$NRMS = \frac{\sigma}{U_b} \times 100 \quad (26)$$

Table 1: RMS percent errors relative to measurements by Sudo et al (1998)

Turbulence Model	NRMS (%)
Standard k- $\epsilon$	15.74
Spalart-Allmaras	18.31
k- $\omega$	15.68
k- $\omega$ SST	14.69
Realizable k- $\epsilon$	14.51
4mm Deflection	13.30
6mm Deflection	8.13

### 3.1.3.1 Potential Impact of Positional Uncertainties

In addition to the possibility that the models employed are failing to capture the pressure gradient in the bend as noted by [15], positional uncertainties may also help explain why there is such a difference between experiment and simulation seen in Figure 17. It may be possible that during the experiment, small deviations in probe positions in the region of large gradients cause significant deviations in measured velocities. There also could have been an averaging effect over measurement volumes, as seen in Figure 10. This effect becomes even more pronounced in regions of very high gradients in which small changes in position lead to large changes in velocity as in the  $r/R < -0.3$  region of Figure 18 it appears to be.

To test this, probe-lines were intentionally deflected in the CFD simulation files and the results were plotted to try to account for the spatial uncertainty expected in the experimental results. They were made by fixing the probe to the center of the pipe and altering the end point on the outer diameter of the pipe to be 4mm and 6mm below that of the centreline to attempt to cover half of the grid spacing observed in experiment as in Figure 10 which can be calculated to be 9mm. The probe lines are visualized in Figure 20. The results of these probe lines are presented in Table 1 as “4mm Deflection” and “6mm Deflection”. It can be seen that there is an improvement from 14.51% to 13.30% to 8.13% when attempted to account for positional uncertainties using the realizable  $k-\epsilon$  model. This

improvement indicates that trying to account uncertainties in the experiment does give a better indication as to how CFD compares to experiment and will be used for subsequent CFD investigations.

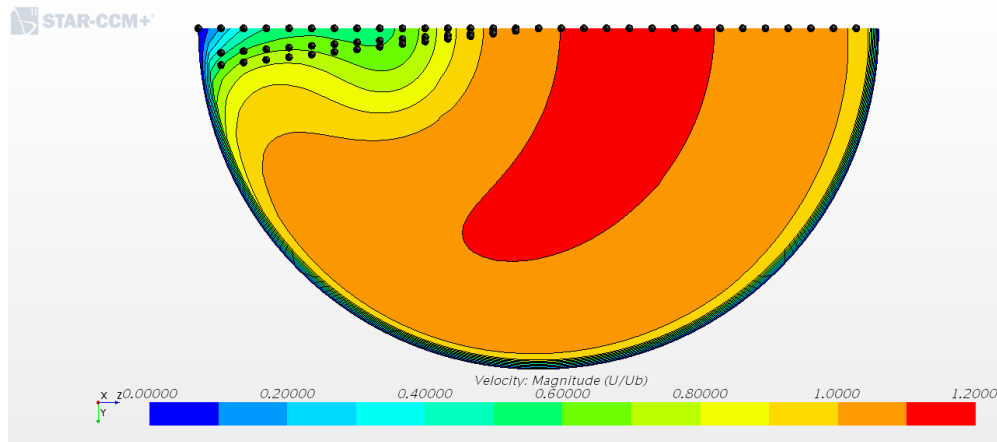


Figure 20: Velocity Contour at the end of the bend displaying the additional 4mm and 6mm deflected probe-lines

The improvement by adding these extra probe lines can be visualized in Figure 21 below. This clearly illustrates that the comparison of only the velocity along the centreline is less accurate for the CFD models. This indicates that attempting to account for measurement volume size and uncertainties that exist in experiments make CFD comparisons more accurate and should help the validation process.. It also shows however that these models still do not capture the gradient measured in the experiment properly which may be a result of these two-equation models failing to handle the swirl associated with the bent pipe flow.

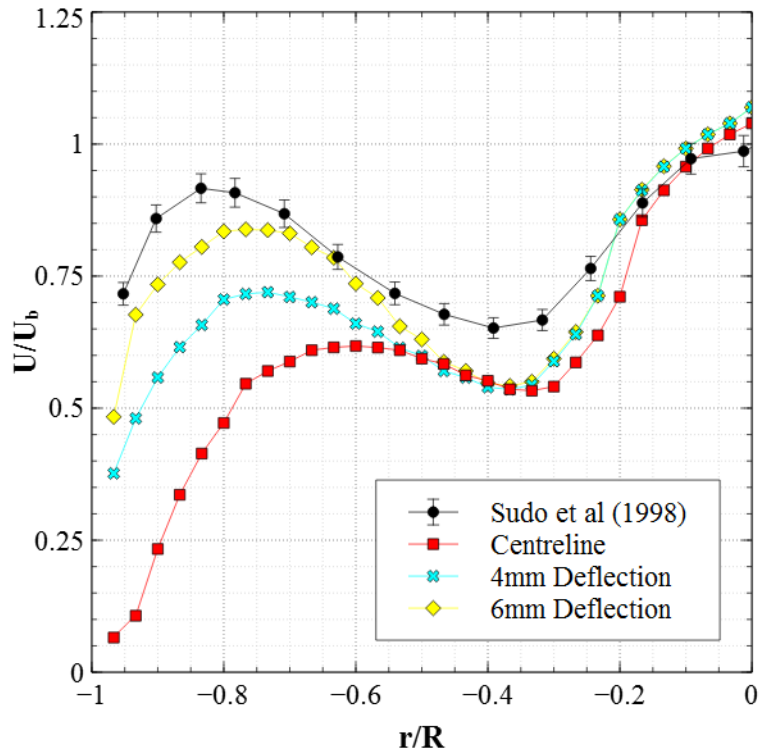


Figure 21: Velocity measurements at outlet of bend with measurements taken from 4mm and 6mm using the realizable  $k-\epsilon$  turbulence model (4.4m node mesh)

### 3.2 Header Assembly Tests

To accurately characterize the velocity field out of the J-nozzles and into the Moderator Test Facility vessel, an accurate set of mass flow rates for each of the nozzles on a header assembly needed to be obtained. This was done by comparing CFD simulations on the header assembly to experimental results on the header assembly. This will determine which turbulence models can be used to accurately determine the mass flow rate for each J-nozzle in the Moderator Flow Test Facility. It should be noted that flow distribution in the manifold can be very

sensitive to the outlet conditions. This experiments outlet conditions differ from the Moderator Flow Test Facility which could have an impact on the flow distribution seen inside the test facility.

### 3.2.1 Geometry Setup

The header assemblies for the Moderator Test facility consist of a manifold, 6-8 J-nozzles and varying lengths of connecting flex hose. These components and assembly are shown in Figure 3 with relevant design values in Table 2.

Table 2: Design Values for Header Assembly

Parameter	Dimension [mm]	Description
ID1	9.398	Inner diameter of main channel
ID2	3.302	Inner diameter of discharge ports
ID3	3.86	Inner diameter of J-Nozzles
L	609.6	Total Length of Manifold
L1	179.6	Distance to centreline of first discharge port
L2	22.86	Length of Discharge Port
L3	120.6	Entry Length to Bend of J-Nozzles
L4	11.3	Exit Length of J-Nozzles
OD3	6.35	Outer Diameter of J-Nozzles
D	35.71	Distance between discharge port centrelines.
IBR	11.05	Inner Bend Radius of J-Nozzles
OBR	17.5	Outer Bend Radius of J-Nozzles
$\theta$	76.0°	Angle of Bend for J- Nozzles

### 3.2.2 Experiment Setup

The header assembly contained a 9.398 mm ID main channel with eight 3.302 mm ID welded discharge ports. Flow was fed from both sides of the main channel for total flow rates of 8, 9 and 10 LPM. To ensure that there was no significant flow imbalance each side had its own Alicat Flow Controller (AFC). This would allow for the flow imbalance to be kept within the uncertainty of these devices. These devices were designed to have a 2% error for their full scale flow rate of 5 LPM [28]. For the flow rate of 9 LPM, this would correspond to each AFC being operated at 4.5 LPM, which would result in an error of 2.2% in each measurement. This corresponds to a total uncertainty of 3.11% in the total flow rate of 9 LPM in this case. All devices used had NIST traceable calibration certificates.

To measure the flow rate of each nozzle, water was collected into a bucket from one nozzle at a time over a 100 s measurement window. This time was chosen to allow for a 0.6% error in timing as the absolute uncertainty in time was determined to be 0.6 s due to reaction times. After the 100 s collection period the bucket was weighed using a scale accurate to 1 g. The mass of the bucket was subtracted off to give an accurate measure of the mass of water collected. As a typical weight of water collected in this 100 s window would be 1.6-2 kg this uncertainty in mass may be neglected giving a total uncertainty in an individual

measurement of 0.6%. Next, after measuring the flow rate of each of these nozzles once, the total flow rate obtained from these eight nozzles was compared to the sum total of the AFCs and a second inline flow meter accurate to 0.5%. This was to ensure that the data obtained was of good quality before collecting more points. Finally, this process was repeated over several days and flow rates to generate repeatability data to test the confidence of these error estimates in addition to the sensitivity of the mass flow distribution to Reynolds Number.

### 3.2.3 Experimental Results

Figure 22 displays the experimental results obtained for a flow rate of 9 LPM. These results were collected in two configurations of the AFCs (AFCs swapped sides for each respective day) to ensure that there were no systematic effects impacting the flow distribution measured due to the AFCs imbalance. It can be seen in Figure 22 that the error band of 0.6% from the average of all points at a given nozzle position appears to be a good representation of the spread in the data.

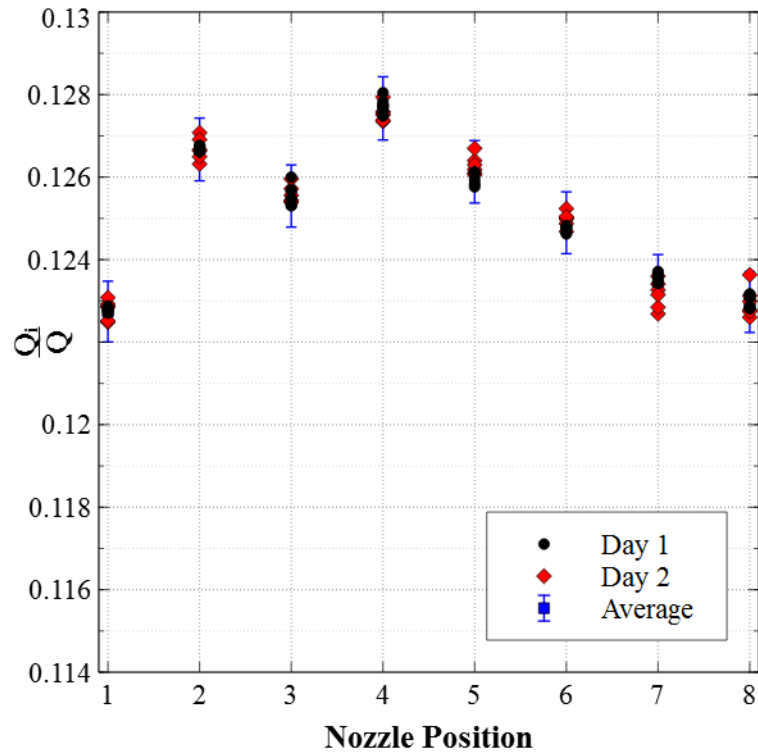


Figure 22: Flow Distribution for Q=9 LPM using both AFC configurations

By referring to Figure 23 it can be seen that no significant difference is observed when varying to total flow rate. This is significant as it means that the predictions for one of the flow rates applies to the whole range relevant to the present study. This will make determining the flow rate for each individual nozzle achievable using one set of predictions.

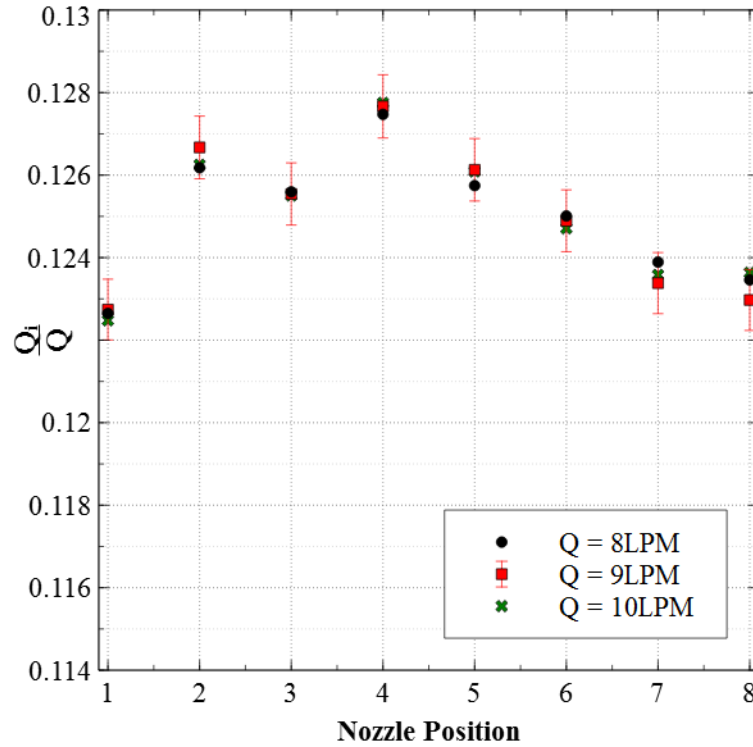


Figure 23: Flow Distribution for all tested total flow rates

### 3.2.4 Discrete Calculation Model

The first method used to compare to experimental results was the discrete method proposed by Acrivos et al [10]. This method is explained in greater detail in section 2.1.

For application to the manifold in the header assembly, it was assumed that there exists perfect symmetry and only half of the manifold needs to be treated. This would leave four discharge ports with five branches. An iterative script was used to predict the pressure and velocity field in the manifold.

### 3.2.5 Header Assembly CFD Setup

The geometry used for CFD simulation of the header assembly was built using the design values specified on Table 2 with one exception. The inner diameter of the discharge ports and flex hose was changed to match that of the J-nozzles. This was done to ensure a controllable wall  $y^+$  in the flex hose and J-nozzle regions. The mesh for this geometry was designed to use the high  $y^+$  wall model and only after ensuring mesh convergence. The default turbulence model used for this study was the realizable  $k-\varepsilon$  model as it was deemed reliable by prior studies by [11].

The mesh was built using the Trimmed cell meshing tool available in STAR-CCM+. By using the custom curve control option and using wake refinements, the grid was refined near the discharge ports to be 12.5% of the total base mesh size. The volume growth rate of the mesh was also chosen to be slow to allow for this region to be sufficiently fine. This mesh can be seen in Figure 24.

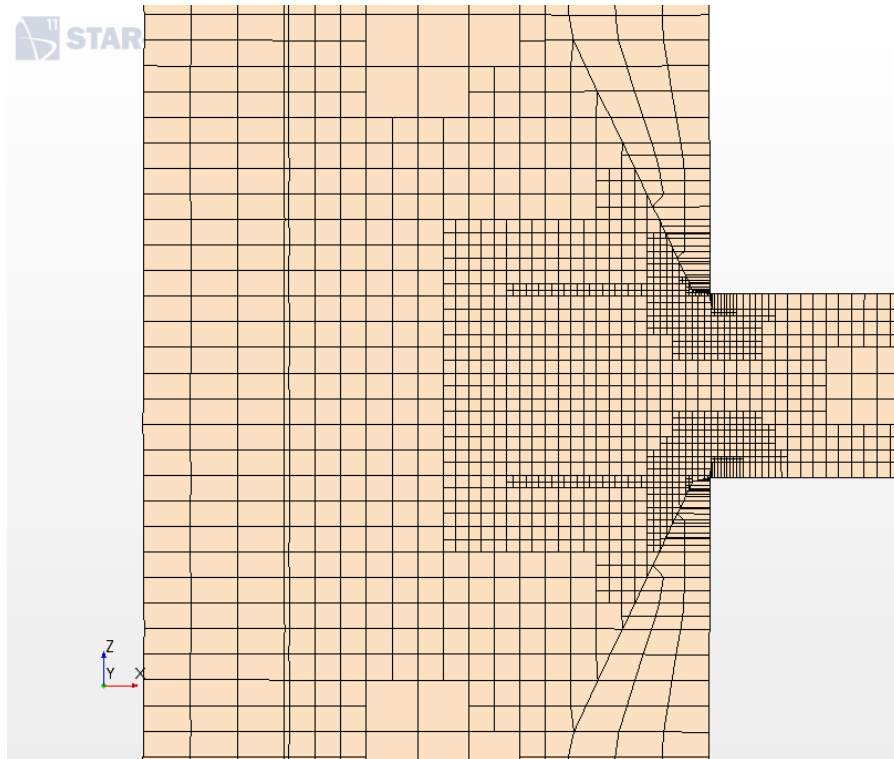


Figure 24: Mesh used in Tee-junction of Manifold

As previously mentioned, only the high  $y^+$  wall model was used for these simulations. As a result it was imperative that the mesh be properly built to ensure a wall  $y^+$  in the range of 20 to 100 to ensure proper use of the model. This was impossible to achieve in some regions of the manifold as flow decelerates significantly as one moves closer to the centre of the manifold. As a result the wall  $y^+$  drops to zero in this region. In light of this, the mesh was designed to have appropriate wall  $y^+$  in the regions before the discharge ports and for the nozzles. This can be visualized in Figure 25. It should be noted that no significant difference was observed when using the all  $y^+$  wall model, as a result the high  $y^+$  wall model was exclusively used.

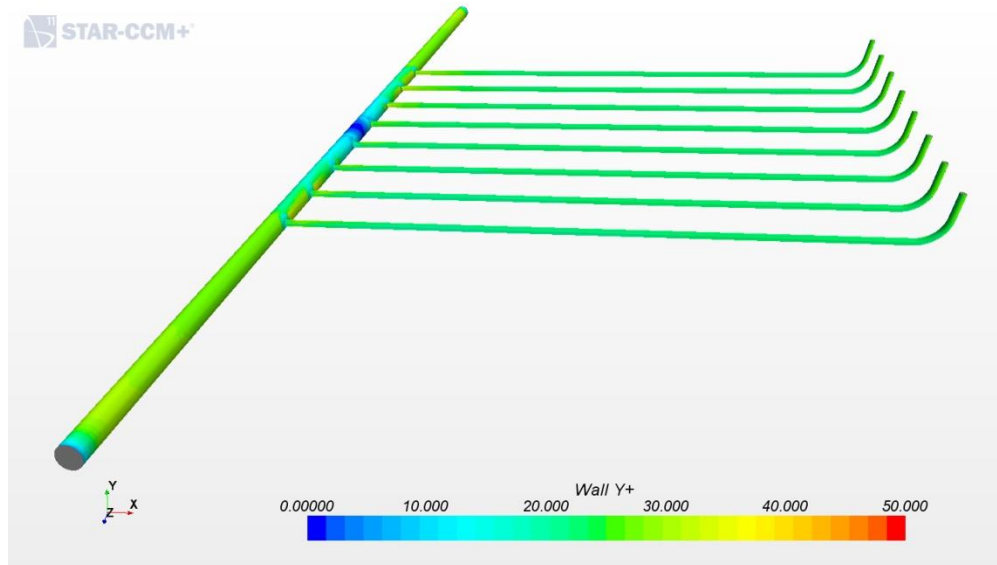


Figure 25: Wall  $y^+$  for Header Assembly simulations

### 3.2.5.1 Mesh Study

To ensure grid sensitivity, four different base mesh sizes were used. Each subsequent base size was half the size of the previous. The results of each of these grids using the realizable  $k-\epsilon$  turbulence model and a uniform inlet velocity distribution (top-hat) for  $Q=9$  LPM can be seen in Figure 26. It can be concluded that there is no significant impact of mesh size on the flow distribution obtained for this mesh layout. This is in part due to the fact that the difference between grid sizes on Figure 26 are negligible compared to the spread in data recorded on Figure 22. As a result, all subsequent simulations were performed using the 0.826 mm base size mesh.

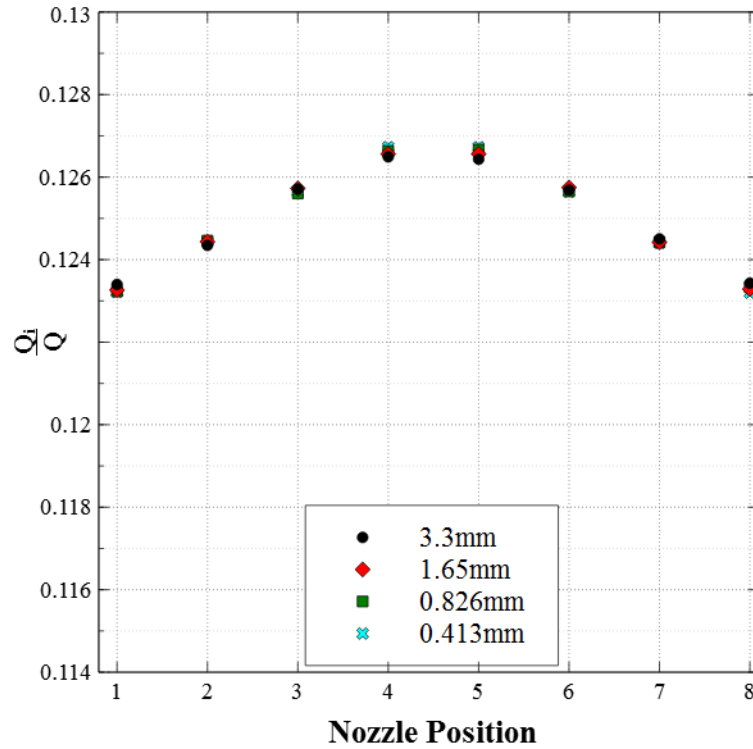


Figure 26: Flow Distribution for various base mesh sizes using realizable k- $\epsilon$

Another important check is to determine the impact of the inlet flow conditions upon the flow distribution obtained. To test this, a fully-developed velocity profile was obtained by creating a periodic boundary condition simulation for a similar grid to avoid interpolation errors. Using this inlet condition and comparing the results to those obtained using a uniform velocity distribution, no significant difference in flow distribution is observed as seen in Figure 27. Therefore, the uniform velocity distribution will continue to be used as it is the simplest to implement and does not result in any difference.

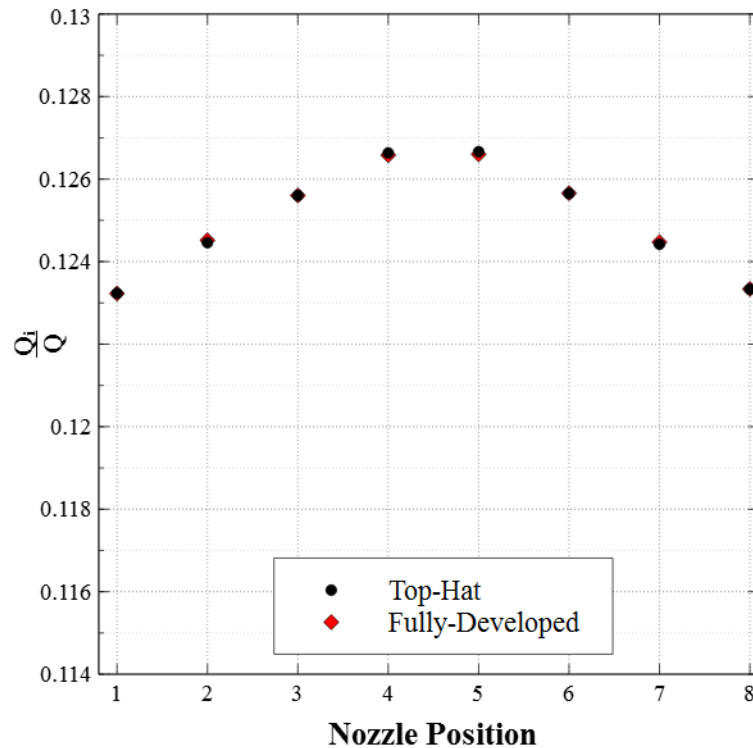


Figure 27: Flow Distribution for Different Inlet Velocity Profiles

### 3.2.5.2 Turbulence Study

Using the 0.826mm base size grid the four candidate turbulence models of standard k- $\epsilon$ , realizable k- $\epsilon$ , k- $\omega$  and k- $\omega$  SST were chosen and the simulations were ran to convergence. These were chosen due to their availability in STAR-CCM+ and due to their popularity in dealing with other types of flows, including the flow expected in the Moderator test facility built at McMaster University. In comparing the flow distributions obtained from these models, it can be seen on Figure 28 that all of the models except for the standard k- $\epsilon$  model give nearly identical results. This is significant as it suggests that k- $\omega$ , k- $\omega$  SST and realizable

$k-\epsilon$  may be interchangeable in determining the flow distribution for dividing manifolds. It must also be noted that only the realizable  $k-\epsilon$  results will be plotted as they are indicative of what the  $k-\omega$  and  $k-\omega$  SST results are.

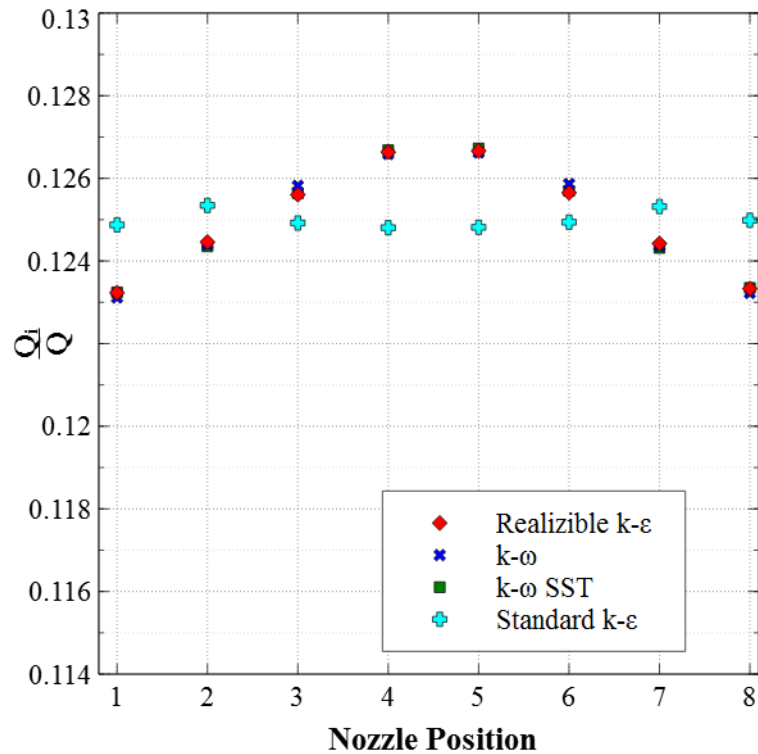


Figure 28: Flow Distribution for various Turbulence Models

### 3.2.6 Comparison to Experiment

Comparison of the discrete model, CFD and experimental results is presented in Figure 29. It is noted that the results of the discrete model closely match those of the realizable  $k-\epsilon$  model. It also can be seen on Figure 29 that the discrete model and realizable  $k-\epsilon$  appear agree within the experimental uncertainty for some but not all the nozzle positions, as the experimental flow distribution appears

asymmetric. This lack of agreement may be a result of defects introduced into the header assembly through the manufacturing process which could act to distort the flow distribution as discussed below.

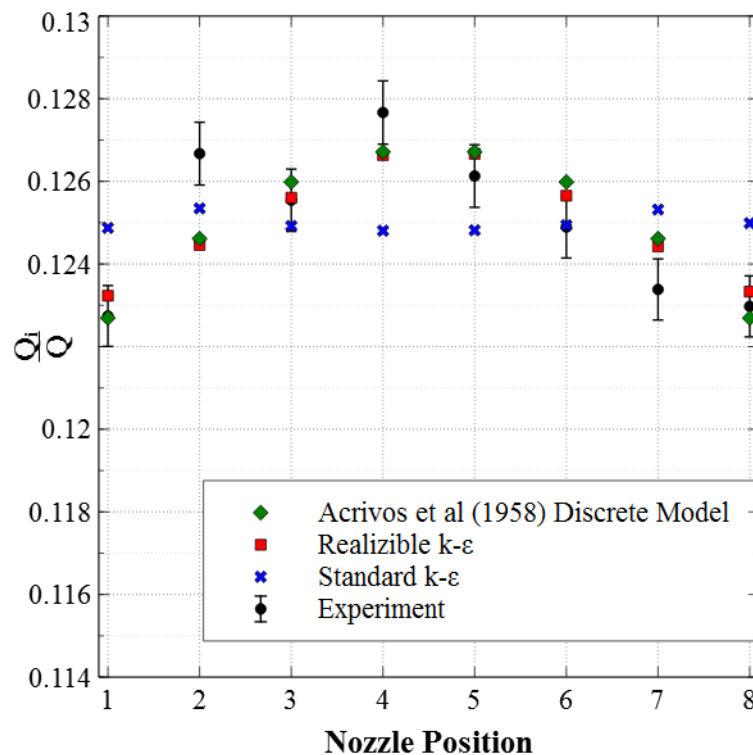


Figure 29: Flow Distribution for various methods

### 3.2.7 Impact of Discharge Port Diameter Tolerances

To assess the impact of manufacturing tolerances on the flow distribution of the manifold, measurements of the discharge port inner diameters were made and a new simulation performed using the as built dimensions. The measured values can

be seen in Table 3. The new simulation did not contain the nozzles and flex hose line. Instead a porous jump was introduced to the simulation to account for the pressure drop across these components to achieve physically accurate outlet boundary conditions. This also allowed for an opportunity to assess the impact of the flex hose and nozzles on the flow distribution as presented in Figure 30.

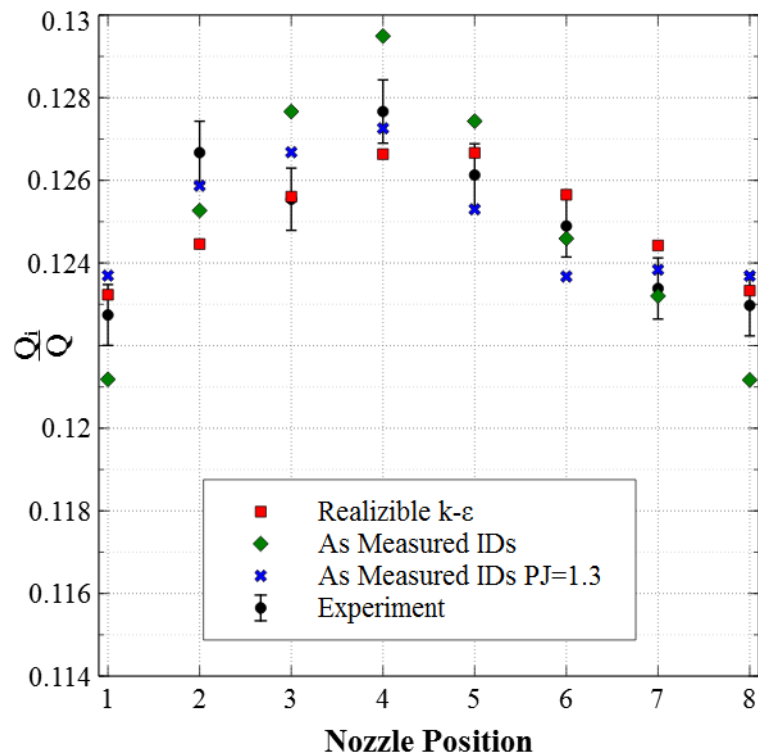


Figure 30: Flow Distribution with inner diameters modified according to measurements

Figure 31 shows the experimental results compared to all of the turbulence models used on the modified inner diameter geometry. It is seen that again the standard k-ε model performs the worst. It should be added that the Acrivos discrete model was not re-calculated due to the assumptions in the model that the

discharge port diameters are uniform. This result shows that CFD is capable of modelling the flow asymmetries when as-built dimensions are used.

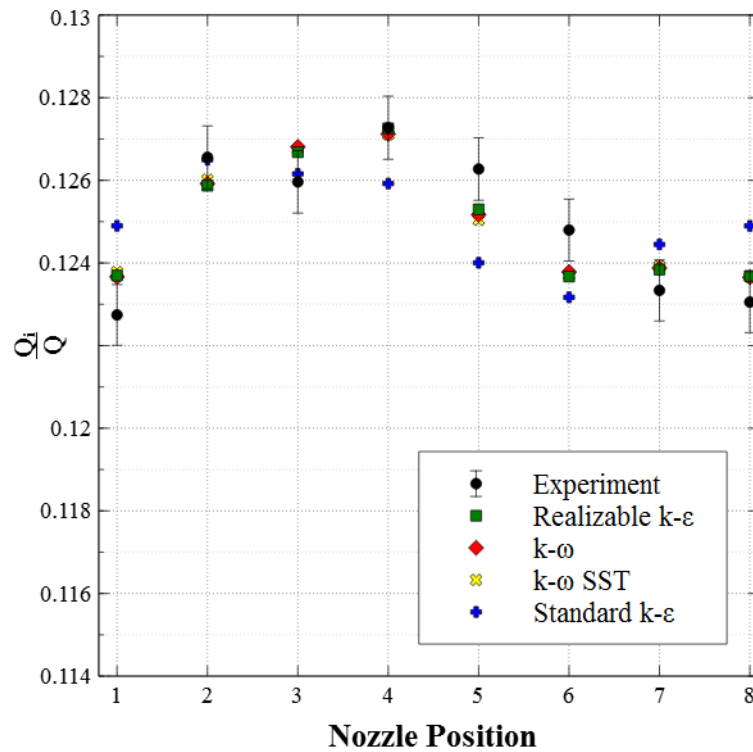


Figure 31: Flow Distribution for various turbulence models using modified inner diameters

### 3.2.8 Validation of Models

To properly validate the calculation models employed in the present study, a figure of merit,  $F$ , was introduced - see equation (27). This value can be interpreted as a fraction from flow uniformity and if the flow field was completely uniform it would yield a value of 1. The intention of this figure of merit is to determine how well a given method determines the maximum and minimum flows in the distribution.

$$F = \frac{\bar{\dot{m}} - \max(\dot{m}_{max} - \bar{\dot{m}}, \bar{\dot{m}} - \dot{m}_{min})}{\bar{\dot{m}}} \quad (27)$$

The obvious flaw of the suggested formulation of F value is that it only tests the maximum and minimum values and does not test the entire distribution. As a result, the RMS error of each point was determined and an average value normalized to the average flow for a model that was calculated and converted to a percentage.

In comparing the figures of merit it can be determined that k- $\omega$ , k- $\omega$  SST, realizable k- $\epsilon$  and discrete model perform best relative to experiment as shown in

Table 4 with the discrete model predicting an F value within uncertainty of experiment. It is of great interest that when the inner diameters of the discharge ports are modified to be consistent with measured values as opposed to design values there is a noticeable improvement in predictive ability as seen in

Table 4.

This means that for subsequent simulations any choice of the  $k-\omega$ ,  $k-\omega$  SST and realizable  $k-\epsilon$  turbulence models would be justified to determine the mass flow distribution to any of the 22 J-nozzles. It also appears than for the most accurate mass flow distribution one would need to determine the K factors for the nozzles and flex hose line in addition to the discharge port inner diameters. These findings are consistent with those of [11] who determined that the realizable  $k-\epsilon$  accurately captures the flow distribution of a manifold fed from one side.

Table 3: Measurements of Discharge Port Inner Diameters

Nozzle Position	Measured Inner Diameter (mm)
1	3.315
2	3.327
3	3.327
4	3.327
5	3.302
6	3.289
7	3.302
8	3.315

Table 4: Performance of each model relative to experiment

Method	F Value	NRMS (%)
Discrete Model	0.982	0.822
k- $\omega$ SST	0.986	0.829
k- $\omega$	0.985	0.836
Standard k- $\epsilon$	0.997	1.39
Realizable k- $\epsilon$	0.986	0.813
Realizable k- $\epsilon$ as measured IDs	0.964	1.18
Realizable k- $\epsilon$ as measured IDs with Porous Jump <sup>5</sup>	0.982	0.688
Standard k- $\epsilon$ as measured IDs with Porous Jump	0.985	1.28
k- $\omega$ SST as measured IDs with Porous Jump	0.983	0.728
k- $\omega$ as measured IDs with Porous Jump	0.983	0.703
Experiment	0.979 $\pm$ 0.006	N/A

### 3.3 J-Nozzle Validation

#### 3.3.1 Experiment Setup

Using the data presented in the previous section, flow rates of 1.1 and 1.5LPM were chosen as they would be indicative of flow rates out of a nozzle on a header assembly with 8 and 6 J-nozzles for a total flow rate of 9LPM. These flow rates correspond to Reynolds numbers of 6800 and 9300 and will give an indication as to the sensitivity of the velocity field of each nozzle in the moderator test facility to Reynolds number. Measurements were made for a horizontal and vertical alignment of the laser plane on the nozzle as can be seen in Figure 32.

---

<sup>5</sup> This porous jump was calculated to be 1.3 as that is the K factor that accounts for the nozzle and flex line losses.

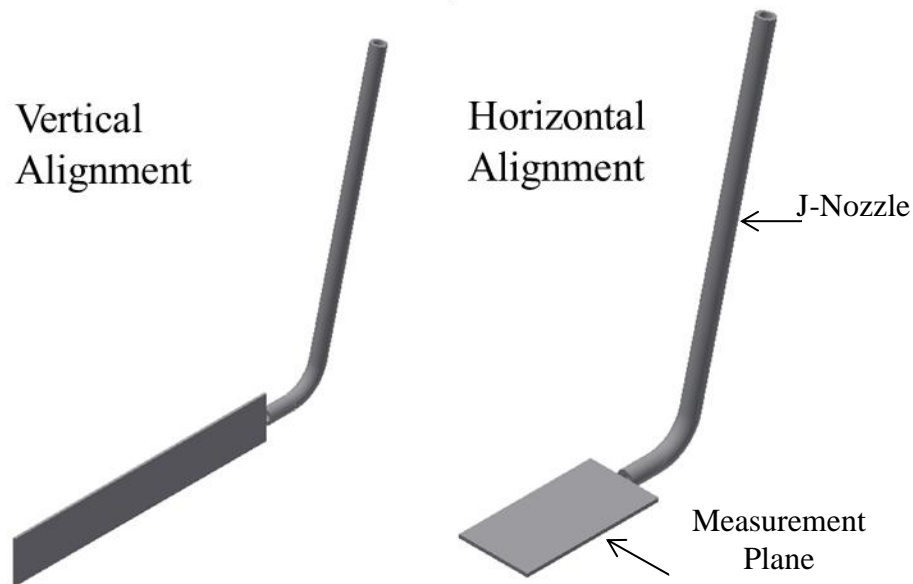


Figure 32: Displays the vertical and horizontal planes measured

The velocity field of the J-nozzles can be measured using various techniques, Particle Image Velocimetry (PIV), Laser Doppler Velocimetry (LDV) and Hot-wire anemometry (HWA) to name a few. More information on these methods can be found in [29]. The chosen method for this study was PIV. It was chosen over HWA due to its availability and that the presence of the hot-wires can distort the flow, which could be a significant issue due to the small size (3.86mm diameter) of the J-nozzle. LDV was not used as there were concerns about the measurement volume size for each measurement and the availability of the equipment. The typical measurement volume size for a LDV measurement is 100  $\mu\text{m}$  (diameter) by 1.3 mm in length [29] which would result in a potentially significant averaging

effect in the axial direction which would need to be accounted for in CFD comparisons.

PIV measures the velocity of a flow field by making use of a pulsed laser, high speed camera and glass particles (“seed”) dispersed in the flow. The laser consists of two beams which are turned into sheets using lenses. This provides an illuminated plane to view seed particles. This is to allow for two images to be captured by the camera (referred to as frames) in quick succession (on the order of  $\mu\text{s}$ ). The presence of the seed allows for a software program to identify individual particles and track their movement from the first frame to the second. This yields an instantaneous velocity measurement of the flow field. It should be noted that an accurate spatial calibration is required to convert the displacement rate of change from pixels/s to a useful unit such as m/s. Figure 33 shows an example of how seed particles might move from frame to frame as seen by the camera.

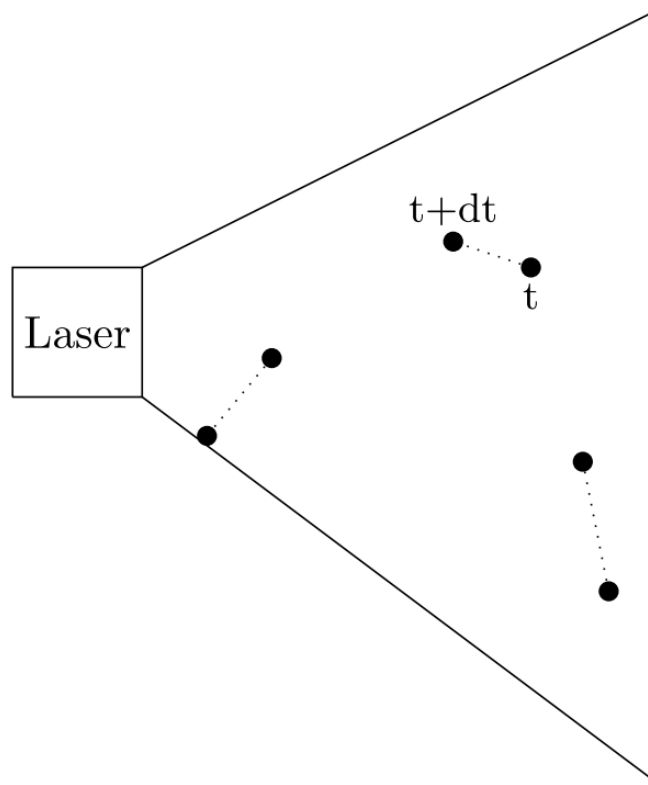


Figure 33: Displays seed particle movement between camera frames

The frequency at which a set of frames is gathered is determined by the camera, which is synchronized with the laser. For example, if one wanted to time average the velocity field with 1000 measurements over 1s we would chose a capture frequency of 1000 Hz. This is important to obtain an accurate time averaged velocity as the frequency of turbulent fluctuations could have a measureable impact on the time averaged velocity field. As a result different capture frequencies should be tested.

Parameters that were found to be of great impact on the quality of data obtained include capture frequency, number of captures, beam thickness, beam positioning, measurement grid and the laser pulse delay.

Beam thickness was found to be a particular issue for these J-nozzles as the thickness of the laser sheet was observed to be roughly 1.5-2mm which is quite large in comparison to the 3.86mm inner diameter of the J-nozzles. In order to reduce this impact, a smaller slit was created using cards to cut the beam to a much more acceptable thickness of 0.5->1mm. This was significant as all seed particles illuminated by the sheet are picked up by the camera. This has an integrating effect on the velocity field and as such the thinner the laser sheet the closer one gets to a measure of only the centreline velocities in either the horizontal or vertical directions.

Beam positioning was also a significant factor since the measurement volume being so small, thus being off even by a seemingly small distance like 1mm would have significant effects on the velocity field measured. The solution to this problem was to create a beam locating device using business cards with several parallel lines drawn on. The intent being that the parallel lines could be used to ensure an adequate beam angle and that the parallel lines be positioned such that one lies on the centreline of the nozzle with another line 1mm to either side to estimate the beam thickness and establish an “at worst” position. A positive

externality of using these cards was that the laser sheet position was much easier to identify.

The laser pulse delay is the time between the first laser turning off and the second laser firing. This can also be interpreted as the time between frames. In the INSIGHT software used to create velocity vectors from the frames one can obtain the percentage of “Good” and “Bad” quality vectors. Good vectors would be characterized by the software clearly identifying seed particles in that grid spacing and tracking them move a maximum of  $\frac{1}{4}$  of the grid spacing. The laser pulse delay ( $dt$ ) was tuned until more than 90% of the vectors in the path of the jet from the J-nozzle were of good quality. For the flow rates of 1.1 and 1.5LPM this corresponded to a value of  $30\mu s$ . It must be noted that this value is not constant for this type of flow as it is highly dependent upon the magnitude of the flow velocity, i.e. the higher the velocities the lower the laser pulse delay and vice-versa.

The seeding concentration for this experiment was determined to allow for 3-6 seed particles to exist in each box composing the measurement grid. A typical seeding profile for these experiments can be seen in Figure 34 and Figure 35 which was deemed acceptable.



Figure 34: Displays the seed for the J-Nozzle Experiments

The grid used for this seeding was 24x24 pixels and can be seen in Figure 35. When processing the data obtained, the “square” grid option in the INSIGHT software was used. This allowed for the data to be processed over this 24x24 grid twice and was found to provide the highest quality data compared to other processing options and grid sizes.

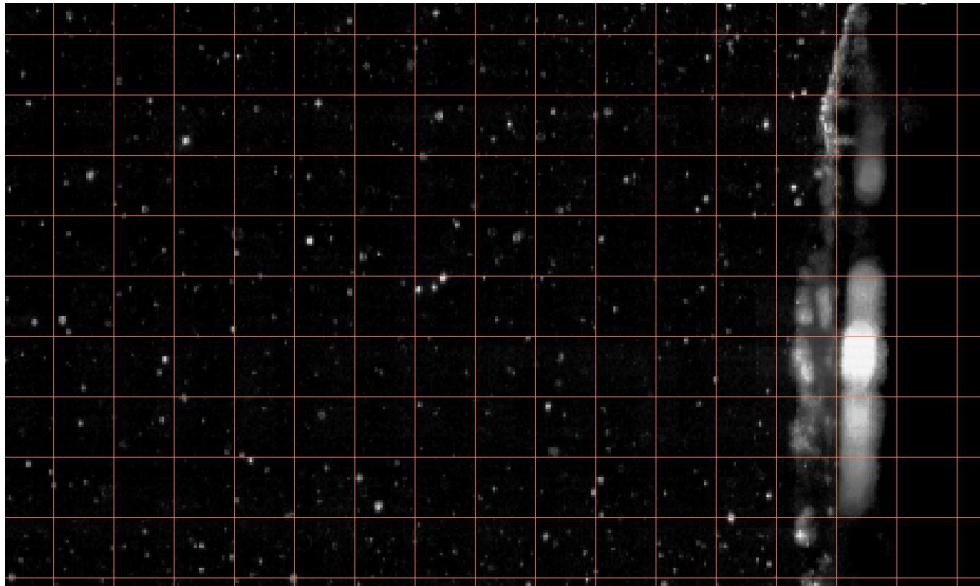


Figure 35: Displays the grid and the number of seed in each grid

### 3.3.2 Results and Repeatability

To estimate the sensitivity of the velocity fields measured to the camera and laser positions, measurements were performed over several days with the laser and/or position being moved and then attempted to be put back in place. These results can be seen for both 1.1LPM and 1.5LPM in both planes in Figure 36 through Figure 39.

In comparing these figures it can be seen that the repeatability is worse for  $Q=1.1\text{LPM}$  as opposed to  $1.5\text{LPM}$ . This is largely attributed to difficulties controlling the lower of the two flow rates. This may be the cause of Figure 36

and Figure 38 having outlying sets of data much lower than the rest (Figure 38 in particular).

To quantify this repeatability, for a capture rate of 500Hz and  $Q=1.5\text{LPM}$ , the maximum and center velocities ( $y=z=0$ ) and integral values were calculated and compared over the several runs. The integral value in Table 5 was calculated using the trapezoid method. It has units of m/s as the integral was obtained using non-dimensionalized positions (i.e.  $y/D$ ). This was performed as different spatial calibrations and camera positions result in different radial positions which makes direct comparison between data difficult.

Table 5: Repeatability Criteria for Vertical and Horizontal plane measurements ( $Q=1.5\text{LPM}$ )

Date (yyyy,mm,dd)	Maximum Velocity (m/s)	Velocity at $y=0$ (m/s)	Integral Value (m/s)
2017/03/13	2.66	2.42	2.71
2017/03/20	2.53	2.28	2.65
2017/03/28	2.59	2.14	2.54
2017/03/29	2.92	2.20	2.54
2017/03/30 Run 1	2.85	2.13	2.51
2017/03/30 Run 2	2.72	2.15	2.28

Using March 20<sup>th</sup> data and March 30<sup>th</sup> Run 1 data in Table 5 as the standard values and normalizing to the bulk fluid velocity of 2.14m/s, an estimate for the percent error in each of the criteria can be calculated and is presented in Table 6.

By taking the maximum of these values, the repeatability and error of these measurements can be taken as 7.57% relative to the March 20<sup>th</sup> and March 30<sup>th</sup> Run 1 data. While 5 to 9% uncertainty seems high, given the size of the nozzle and pixel dimensions such repeatability is acceptable.

Table 6: Normalized RMS Percent errors for repeatability criteria (Q=1.5LPM)

	Maximum Velocity	Velocity at y=0	Integral Value
NRMS Horizontal Plane (%)	4.93	6.66	3.23
NRMS Vertical Plane (%)	4.79	2.48	7.57

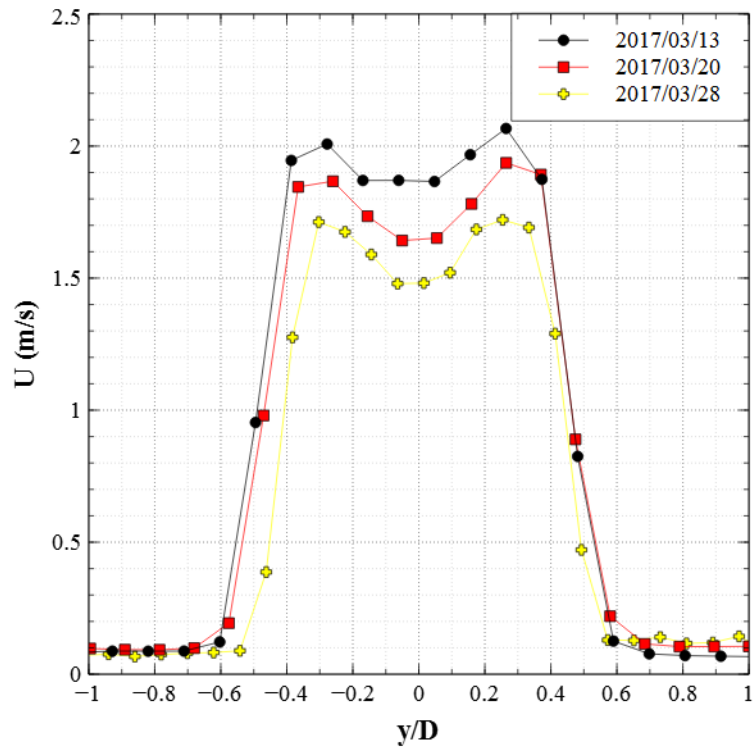


Figure 36: PIV Results - Horizontal Plane Measurements at Q=1.1LPM and 500Hz capture frequency

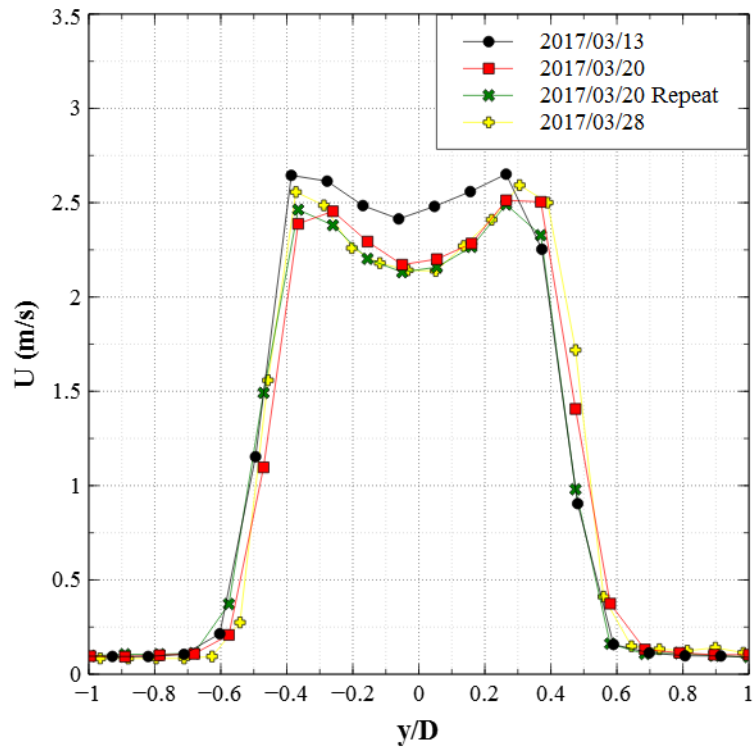


Figure 37: PIV Results - Horizontal Plane Measurements at  $Q=1.5\text{LPM}$  and 500Hz capture frequency

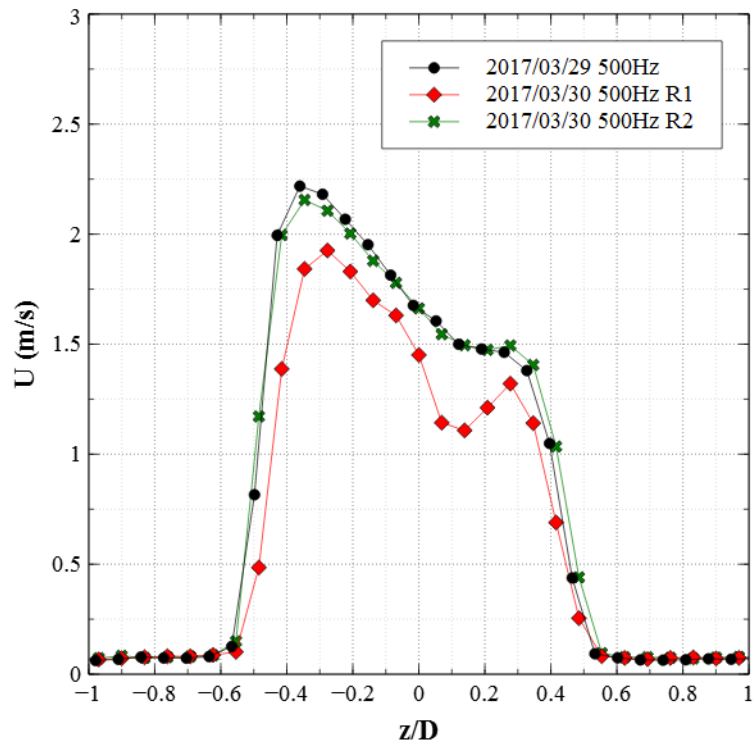


Figure 38: PIV Measurements - Vertical Plane at  $Q=1.1$ LPM 500Hz capture frequency

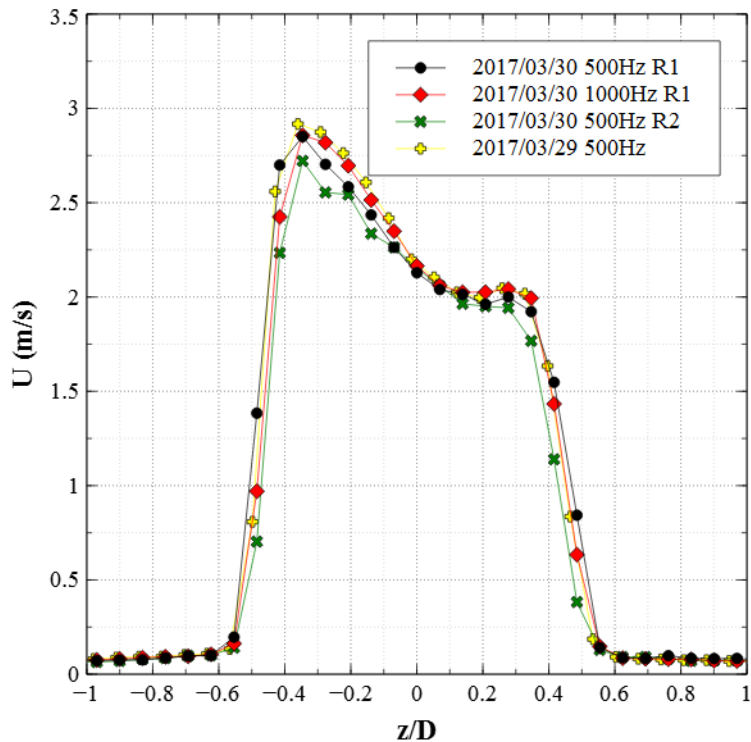


Figure 39: PIV Measurements - Vertical Plane at  $Q=1.5\text{LPM}$

### 3.3.3 Effects of Flow Rate

By normalizing the respective flow distribution by its average velocity (normalized bulk velocity) a determination of the impact of Reynolds number on the velocity distribution can be made. This was done for both planes and it was shown that there is no significant difference between the two flow rates as shown in Figure 40 and Figure 41 respectively. It must be noted that it was decided to use PIV results from the same day and laser/camera positions to ensure that errors associated with positioning the equipment did not skew the comparison to be artificially poor. The error bars on Figure 40 and Figure 41 were generated using

an estimated uncertainty in the flow rate of 0.05LPM due to flow oscillations which workout to be 4.5% and 3.3% for 1.1 and 1.5LPM respectively. This result is significant as it indicates that for each of the 22 J-nozzles used in the moderator test facility, the flow distribution out of each nozzle will be very similar. This would allow for a single velocity field to be used for each nozzle provide the magnitudes are tuned to be consistent with the mass flow of a nozzle in each particular position.

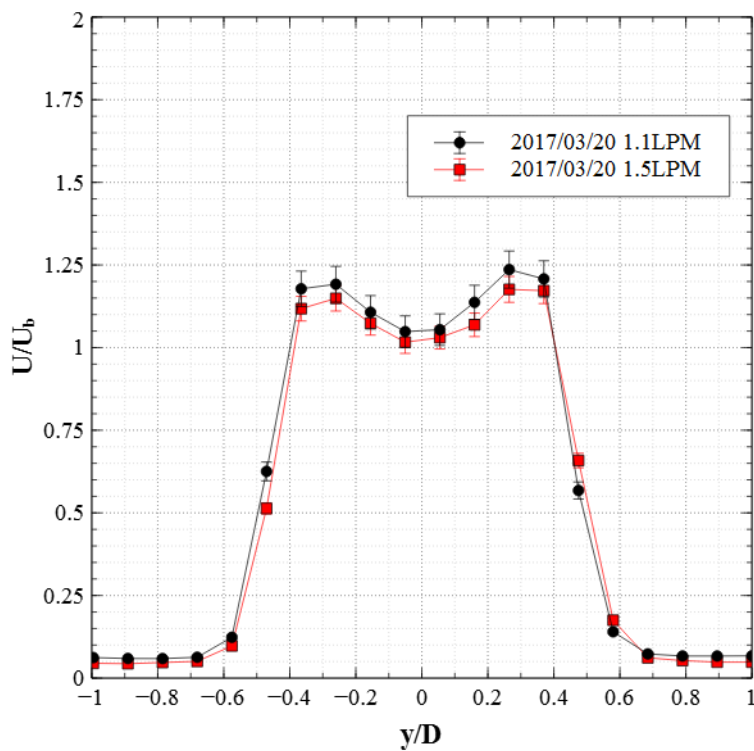


Figure 40: PIV Results - Normalized Horizontal Velocity comparison

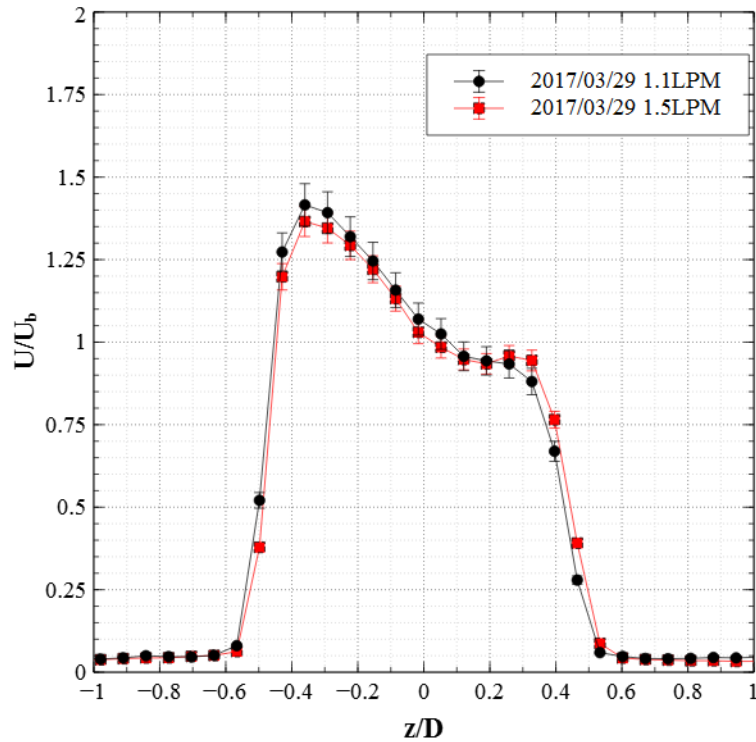


Figure 41: Normalized Vertical Plane Velocity Measurements

### 3.3.4 CFD Setup

The grids used for the simulations was also generated using the Trimmed cell mesher in STAR-CCM+. To ensure a good quality mesh in the region of the jet, wake refinements were performed to 100% of the base size in the vicinity of the jet and nozzle. The mesh used can be seen in Figure 42.

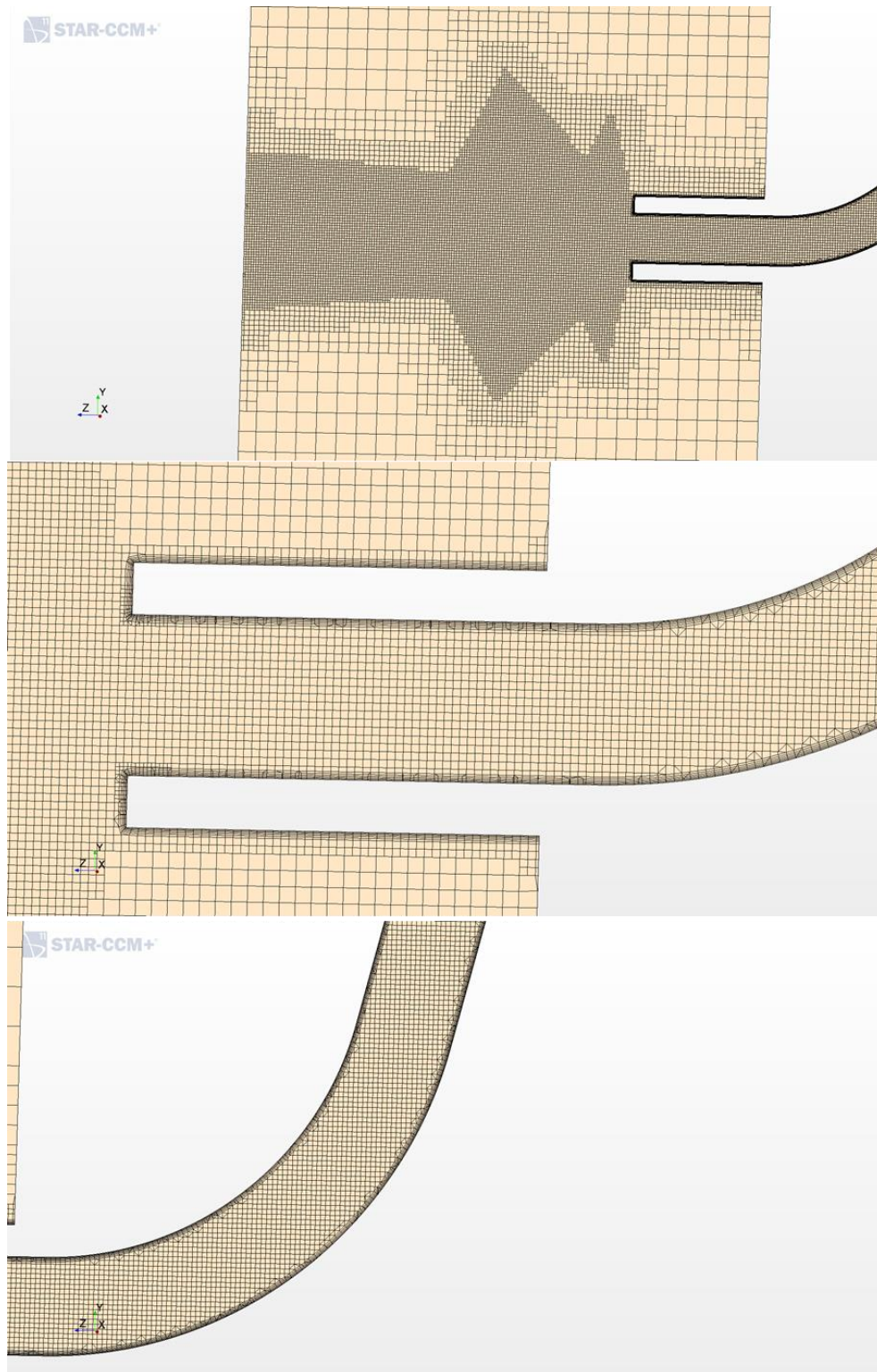


Figure 42: Mesh with 0.193mm base size used for J-nozzle simulations

Due to the small size of the nozzle, it was decided that the low  $y^+$  wall model should be tested. As a result, the wall  $y^+$  of the no-slip walls needed to be tuned to fall within the  $0 < y^+ < 5$  region. This was done by choosing a prism thickness layer for the boundary layer and simulating and adjusting until it gave a desirable  $y^+$ . This was found to be a prism layer thickness of 0.193 mm with 6 layers and a growth factor of 1.2. The wall  $y^+$  for this boundary layer setup can be seen on Figure 43 below and it can be seen that the  $y^+$  falls within the desired range. The size of the fluid volume used was 4x4x4cm and it was found that using a 6x6x6cm fluid volume had no significant impact on the results obtained. As a result, all of the results were obtained using the 4x4x4cm fluid volume.

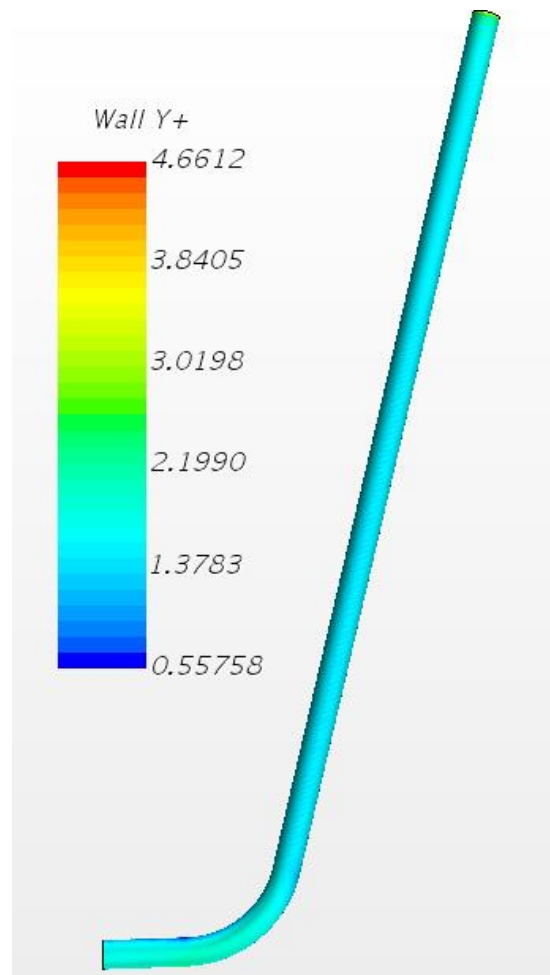


Figure 43: Wall  $y^+$  for J-Nozzle Simulations ( $Q=1.5\text{LPM}$ )

#### 3.3.4.1 Mesh Study

A mesh study was performed to ensure that the solutions obtained are grid-insensitive. To test this, three grids were generated and solved using the realizable  $k-\epsilon$  turbulence model. The three base sizes used were 0.386, 0.193 and 0.0965 mm and the results for both the horizontal and vertical planes can be seen in Figure 44 and Figure 45. Looking at these figures, it can be concluded that using a base size of 0.193 mm would be justified as differences between grids from that

base size are insignificant compared to the estimated 7.57% uncertainty in the experimental results. For an additional check, the  $k-\omega$  SST model was also used and no significant difference between meshes was found. As a result for future simulations, the 0.193 mm base size mesh will be used exclusively.

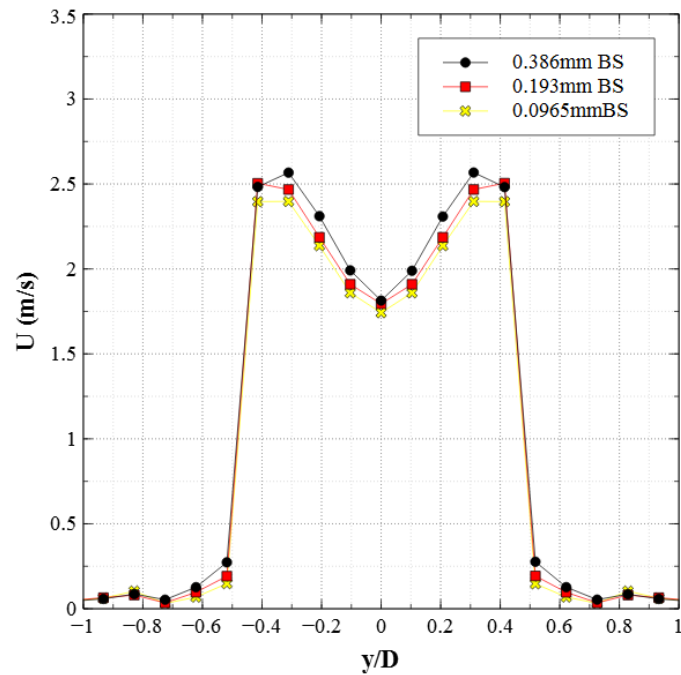


Figure 44: Mesh Study- Velocity Field along Horizontal Centreline using realizable  $k-\epsilon$

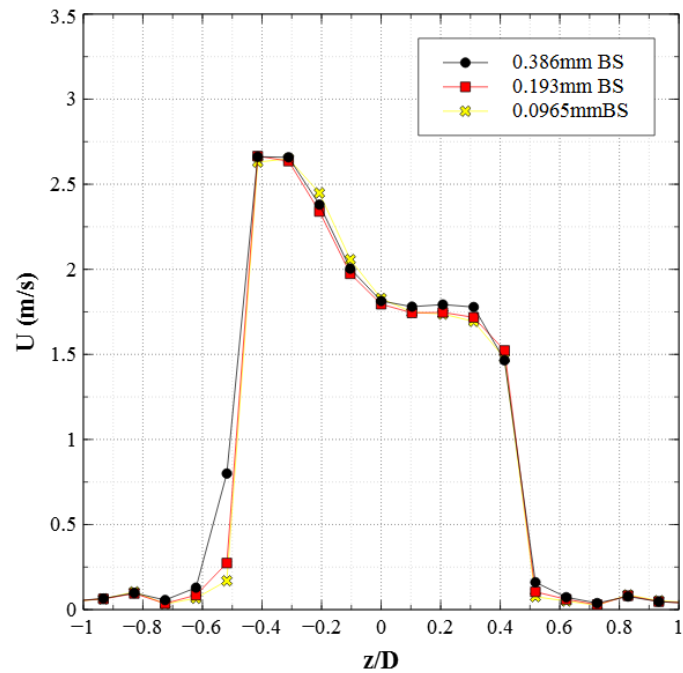


Figure 45: Mesh Study - Velocity Field along vertical centreline using realizable  $k-\epsilon$

### 3.3.4.2 Inlet Boundary Condition Test

Various inlet boundary condition were tested to ensure that there is no significant effect on the results, or if there is that it is well understood. This was done by recreating the nozzle geometry to have 100 pipe diameters of entry length to ensure a fully developed profile into the bend. The results of this compared to the normal unmodified geometry ( $\sim 30D$  of entry) can be seen in Figure 46 and Figure 47 and it is noted that no significant effect can be observed. This was done for a mesh base size of 0.193mm using the realizable  $k-\epsilon$  turbulence model.

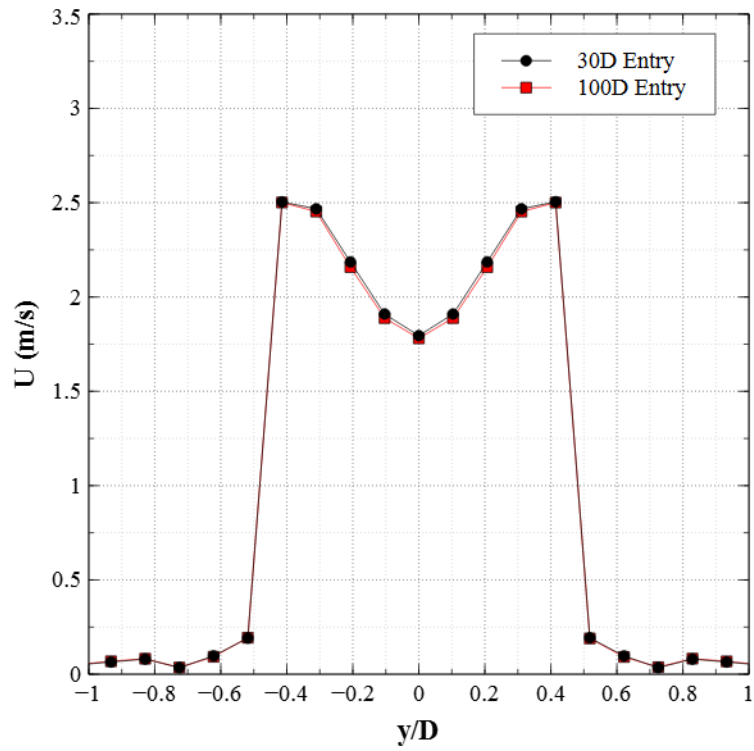


Figure 46: Inlet Boundary Condition Test - Horizontal Velocity Field

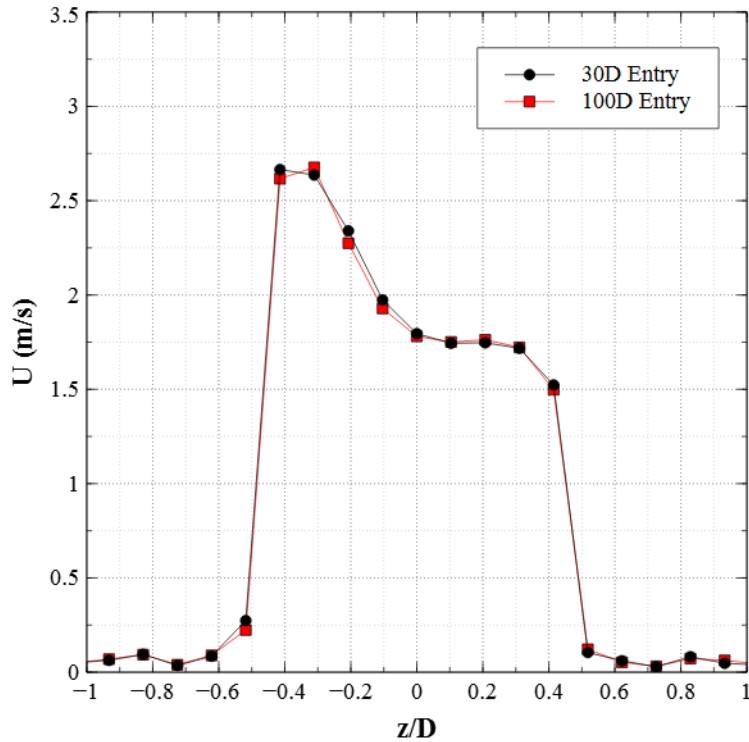


Figure 47: Inlet Boundary Condition Test - Vertical Velocity Field

### 3.3.4.3 Turbulence Model Studies

In order to obtain accurate CFD results, one must test over a wide range of turbulence models as different models capture different flow phenomena better than others. The  $k-\omega$ ,  $k-\omega$  SST, realizable  $k-\epsilon$  and standard  $k-\epsilon$  models were all used on the 0.193mm base size grid. The calculated results using these models can be seen on Figure 48 and Figure 49 and it is apparent that the standard  $k-\epsilon$  model resolves the gradients in the flow field in a manner different than the other models.

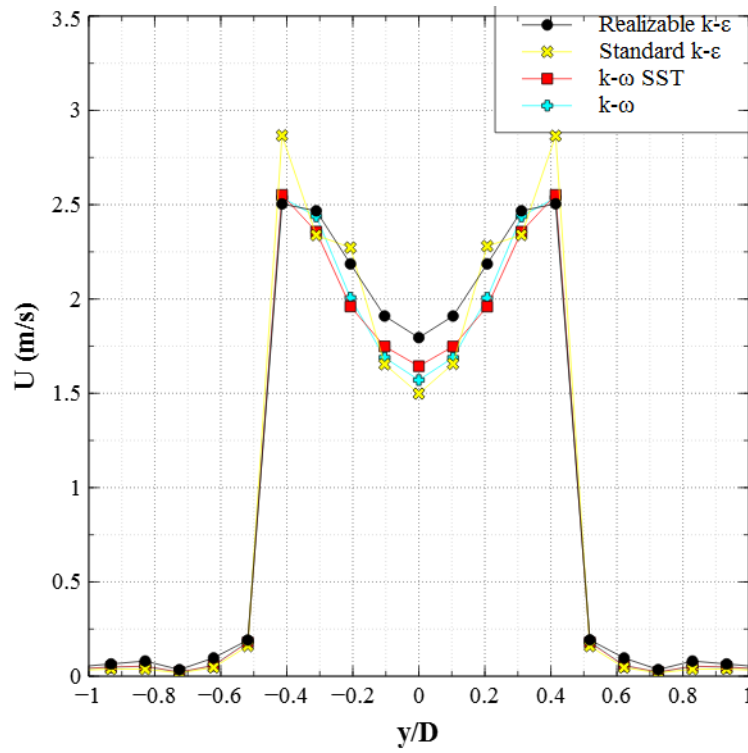


Figure 48: Turbulence Study - Velocity along Horizontal Plane

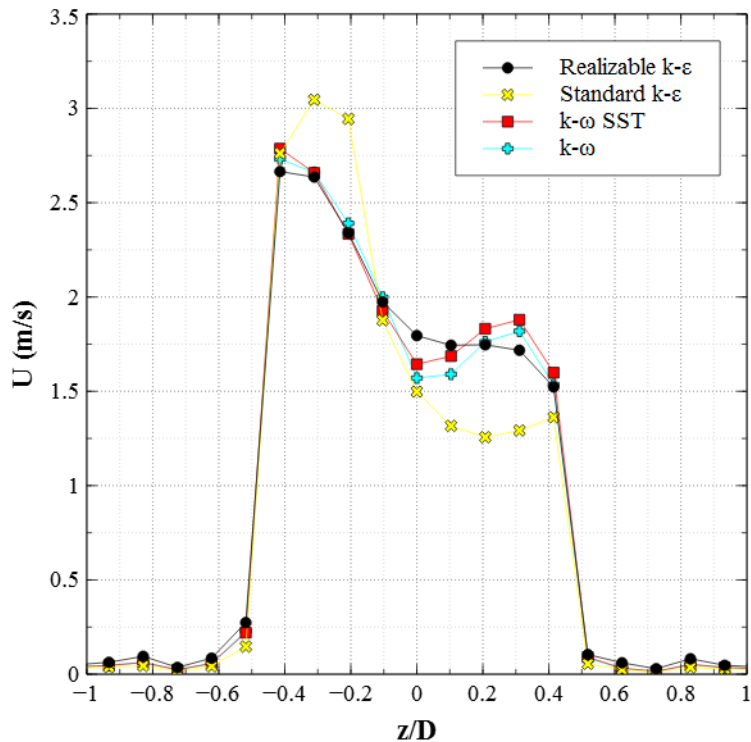


Figure 49: Turbulence Study - Velocity along Vertical Plane

### 3.3.5 Comparison to Experiment

To properly compare the CFD calculations to experiment, it was decided that the positional uncertainty needed to be taken into account. This is because the integrating effect that the beam thickness provides in PIV is not seen in CFD as one has very good control of where velocities are being predicted in CFD software's such as STAR-CCM+. In an attempt to remedy this, additional probe lines were generated 0.5 mm to either side of the horizontal and vertical centrelines in an attempt to capture the integrating effect that the beam thickness

has in experimental results. The positions of these probe lines are shown in Figure 50. Plots containing the extra probe lines can be seen in Figure 51 and Figure 52 for the realizable k- $\epsilon$  model to indicate how the velocity field can vary within  $\pm 0.5\text{mm}$ . The results of CFD relative to experiment can be seen in Table 7 below. These results were compared by computing the RMS error and normalizing to the bulk fluid velocity to get a percent error. It is noted that the model that performs the best overall is the realizable k- $\epsilon$  model compared to the other models as shown in Table 7. It can also be seen that averaging the results over the estimated thickness of the beam improves the agreement with experiment in most cases - see Table 7. This supports the suggestion that for proper CFD validation measurement volumes and positional uncertainties need to be taken into account.

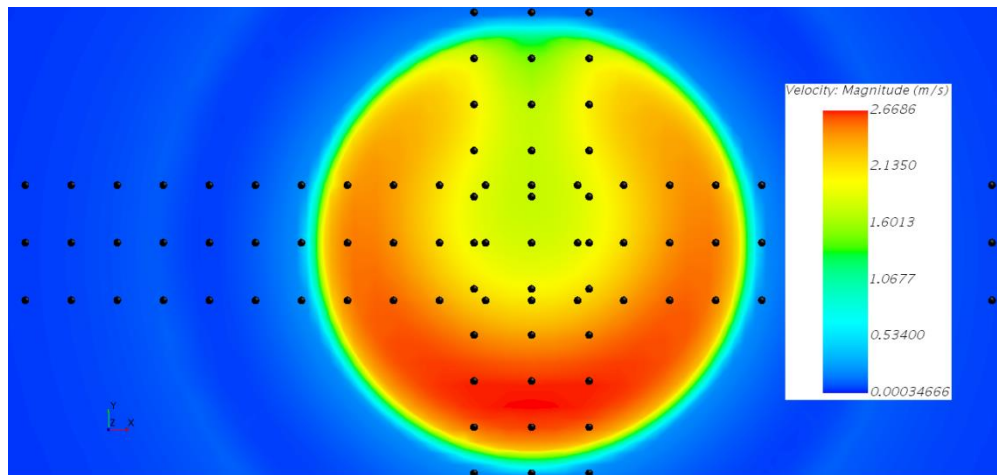


Figure 50: Velocity Contour of J-Nozzle outlet using realizable k- $\epsilon$  (Q=1.5LPM)

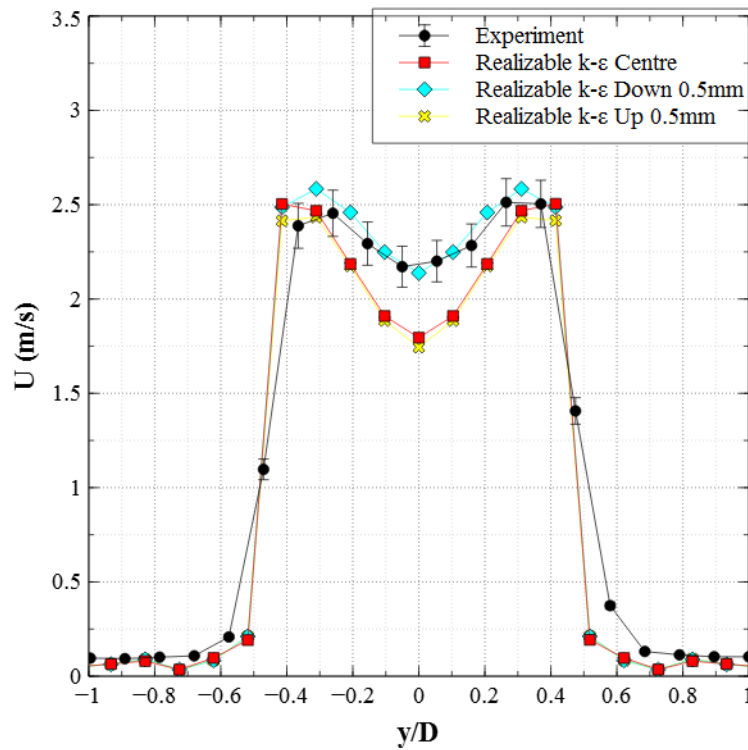


Figure 51: Horizontal Velocity Profile - Experiment compared to realizable k-ε

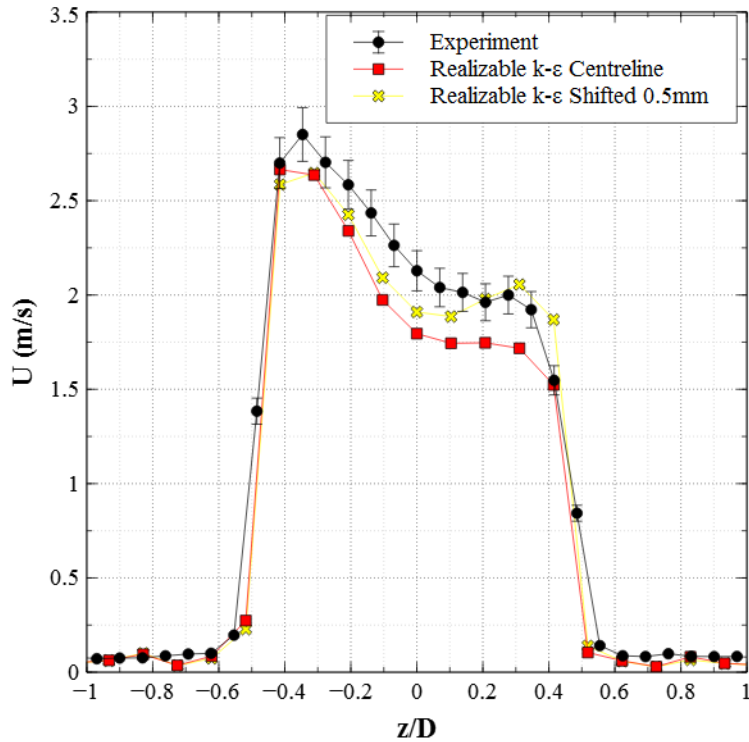


Figure 52: Vertical Velocity Profile - Experiment compared to realizable k- $\epsilon$

Table 7: NRMS Error values for CFD models relative to experiment

Method	NRMS Vertical (%)	NRMS Horizontal (%)
Standard k- $\epsilon$	14.6	16.4
Standard k- $\epsilon$ Averaged	15.1	8.02
Realizable k- $\epsilon$	7.66	13.6
Realizable k- $\epsilon$ Averaged	8.21	7.33
k- $\omega$	12.5	16.9
k- $\omega$ Averaged	8.47	9.20
k- $\omega$ SST	12.7	16.7
k- $\omega$ SST Averaged	8.24	9.36

## 4 FUTURE WORK

### 4.1 Improved Nozzle Velocity Field Measurements

As previously mentioned, the beam thickness of the laser is a significant fraction of the total flow area of the nozzle. As a result, a significant averaging effect occurs and blurs the data together. Although this was resolved by averaging in the CFD simulations, a better solution to this problem would be to design larger nozzles while maintaining the same non-dimensional distances and the Reynolds number. For example, if a 7.75mm ID tube were used instead, this 0.5-.1mm laser sheet would have a much smaller averaging effect relative to the size of the tube. This would also improve the repeatability of the experiment as a larger target to set the laser at would make alignment of the beam easier.

Additional measurements using higher frequencies such as 2000 and 4000Hz could be performed in the future. This would add more data to determine the impact of high frequency turbulent fluctuations on the time averaged results.

Another potential improvement for future velocity measurements would be the use of Laser Doppler Velocimetry (LDV). The main difference between LDV to PIV is that LDV would provide point measurements. This would allow for multiple measurements of the velocity field just outside the nozzle outlet and potentially provide more useful measurements than PIV as the outlet of the nozzle

was the most important area to measure. This would also be improved if a larger nozzle was used.

#### 4.2 Additional Separate Effects Study

In addition to the effects studied in this report it would be of great interest to examine the impingement of one of these nozzles on an unheated and heated element indicative of the moderator test facility at a distance of 20 to 40 pipe diameters away. This would give a more detailed understanding of how the flow field interacts with the heated elements at a distance typical of the moderator facility.

#### 4.3 Simulation of Additional Header Assemblies

As it was found in section 3.2.7 the realizable k- $\epsilon$  turbulence model with an accurate set of discharge port inner diameter measurements very accurately predicts the mass flow distribution additional simulations of the three header assemblies not examined could be performed. This would give a full set of flow rates for each header assembly which could then be used in subsequent simulations as part of the inlet flow conditions of the moderator test facility. It should also be noted that if the discharge port inner diameter were larger, than the diameters could be made to a much higher degree of accuracy. This would result in a more symmetrical flow distribution and would also allow for the other header assemblies to be predicted using the Acrivos et al [10] discrete model.

## 5 CONCLUSIONS

This study was designed to support future work on the Moderator Test Facility by characterizing the inlet flow conditions into the vessel. An accurate set of inlet flow conditions were required to ensure that if the temperature and velocity fields of the tank do in fact have some dependency on the mass flow distribution and velocity field that they can be accounted for in CFD simulations. This was done by performing in house experiments and simulations to determine if the standard  $k-\epsilon$ , realizable  $k-\epsilon$ ,  $k-\omega$  or  $k-\omega$  SST models are interchangeable or if there is one that performs better than the rest.

It was determined that the inlet flow conditions of the moderator test facility can be accurately determined by using the realizable  $k-\epsilon$  turbulence model. This was determined as this model routinely resulted in the lowest percentage of error when compared to experiment in the same way as other turbulence models. It should also be noted that  $k-\omega$  and  $k-\omega$  SST also provide accurate predictions and could be used instead of realizable  $k-\epsilon$ .

It was also shown that the accuracy of CFD predictions can be greatly improved by attempting to account for manufacturing tolerances observed in the header assemblies. This was found to be the most accurate method of calculating the flow distribution of the header assembly when used with a calibrated porous jump

constant of 1.3, which accurately captured the pressure losses of the nozzles and flex hose lines.

The effects of positional uncertainties and measurement volumes were also examined by averaging CFD results over the same estimated area that the experimental results were taken in. This was found to have a significant impact as most models performed much better relative to experiment when attempting to account for the beam thickness in the PIV measurements.

In examining the velocity field of the J-nozzles, it was found that there is no significant difference between flow rates of 1.5 and 1.1LPM. This means that for subsequent simulations the same inlet velocity field may be used for each of the 22 J-nozzles. The velocity magnitudes would need to be scaled down to be consistent with the actual mass flow rate of each J-nozzle and the chosen flow rates for the header assemblies.. It was also found that using the realizable  $k-\epsilon$  turbulence model coupled with accurate measurements of the discharge port inner diameters give a very accurate measurement of what the mass flow rate to each J-nozzle will be. This means that each header could be measured and simulated to obtain a flow rate for each of the 22 J-nozzles.

## 6 Bibliography

- [1] Canadian Nuclear Safety Commission, Candian Nuclear Safety Commission, 20 01 2016. [Online]. Available: <http://nuclearsafety.gc.ca/eng/reactors/power-plants/nuclear-power-plant-safety-systems/index.cfm>. [Accessed 21 04 2017].
- [2] M.Kim, S.Yu and H.Kim, "Analyses on fluid flow and heat transfer inside Calandria vessel of CANDU-6 using CFD," *Nuclear Engineering and Design*, vol. 236, pp. 1155-1164, 2006.
- [3] C.Yoon, B.Rhee and B.Min, "3-D Analysis of the CANDU-6 Moderator Circulation Under Nnormal Operating Conditions," *Journal of the Korean Nuclear Society*, vol. 36, no. 6, pp. 559-570, 2004.
- [4] H.K.Versteeg and W.Malalasekera, *An Introduction to Computational Fluid Dynamics The Finite Volume Method*, Harlow: Pearson Educated Limited, 2007.
- [5] D.C.Wilcox, *Turbulence Modelling for CFD*, DCW Industries, Inc, 2006.
- [6] T.Shih, W.Liou, A.Shabbir, Z.Yang and J.Zhu, "A New k-e Eddy Viscosity Model for High Reynolds Numer Turbulent Flows-Model Development and Validation," *NASA Technical Memorandum*, pp. 1-30, 1994.

- [7] CD-adapco, "STAR-CCM+ User Guide," CD-adapco.
- [8] H.Tennekes and J.L.Lumley, A First Course in Turbulence, Cambridge, Massachusetts and London, England: The MIT Press, 1972.
- [9] B.Launder and D.Spalding, "The Numerical Computation of Turbulent Flows," *Computer Methods in Applied Mechanics and Engineering*, vol. 3, pp. 269-289, 1974.
- [10] A.Acrivos, B.Babcock and R.Pigford, "Flow Distribution in Manifolds," *Chemical Engineering Science*, vol. 10, pp. 112-124, 1959.
- [11] A.Chen and E.Sparrow, "Turbulence Modelling for flow in a distribution manifold," *International Journal of Heat and Mass Transfer*, vol. 52, pp. 1573-1581, 2009.
- [12] A.Tomor and G.Kristof, "Validation of a Discrete Model for Flow Distribution in Dividing Manifolds: Numerical and Experimental Studies," *Periodica Polytechnica Mechanical Engineering*, vol. 60, pp. 41-49, 2016.
- [13] J.Wang and H.Wang, "Discrete method for design of flow distribution in manifolds," *Applied Thermal Engineering*, vol. 89, pp. 927-945, 2015.
- [14] J.Wang, "Theory of flow distributions in manifolds," *Chemical Engineering Journal*, vol. 168, pp. 1331-1345, 2011.
- [15] R.Bajura, "A Model for Flow Distribution in Manifolds," *Journal of Engineering Power*, pp. 7-12, 1971.
- [16] J.Wang, Z.Gao, G.Gan and D.Wu, "Analytical Solution of flow coefficients

- for a uniformly distributed porous channel," *Chemical Engineering Journal*, vol. 84, pp. 1-6, 2001.
- [17] K.Sudo, M.Sumida and H.Hibara, "Experimental investigation on turbulent flow in a circular-sectioned 90-degree bend," *Experiments in Fluids*, vol. 25, pp. 42-49, 1998.
- [18] J.Kim, M.Yadav and S.Kim, "Characteristics of Secondary Flow Induced by a 90-Degree Elbow in Turbulent Pipe Flow," *Engineering Applications of Computational Fluid Mechanics*, vol. 8, no. 2, pp. 229-239, 2014.
- [19] M.Enayet, M.Gibson, A.Taylor and M.Yianneskis, "Laser-Doppler measurements of laminar and turbulent flow in a pipe bend," *International Journal of Heat and Fluid Flow*, vol. 3, no. 4, pp. 213-219, 1982.
- [20] P.Dutta, S.K.Saha and N. N.Nandi, "Numerical study of flow separation in 90-degree pipe bend under high Reynolds number by k-e modelling," *Engineering Science and Technology, an International Journal*, vol. 19, no. 2, pp. 904-910, 2016.
- [21] K.Sudo, M.Sumida and H.Hibara, "Experimental investigation on turbulent flow through a circular-sectioned 180-degree bend," *Experiments in Fluids*, vol. 28, pp. 51-57, 2000.
- [22] L.Boguslawski and Cz.Popiel, "Flow Structure of the free round turbulent jet in the initial region," *Journal of Fluid Mechanics*, vol. 90, pp. 531-539, 1979.

- [23] G.Xu and R.Antonia, "Effect of different initial conditions on a turbulent round free jet," *Experiments in Fluids*, vol. 33, pp. 677-683, 2002.
- [24] B.Boersma, G.Brethouwer and F.Nieuwstadt, "A numerical investigation on the effect of the inflow conditions of the self-similar region of a round jet," *Physics of Fluids*, vol. 10, no. 4, pp. 899-909, 1998.
- [25] N.Georgiadis, D.Yoder and W.Engblom, "Evaluation of Modified Two-Equation Turbulence Models for Jet Flow Predictions," in *44th AIAA Aerospace Sciences Meeting and Exhibit*, Reno, Nevada, 2006.
- [26] E.Smith, J.Mi and B.Daily, "Preliminary Examination of a "Round Jet Initial Condition Anomaly" for the k-e Turbulence Model," in *15th Australasian Fluid Mechanics Conference*, Sydney, Australia, 2004.
- [27] P.Roache, "Perspective: A Method for Uniform Reporting of Grid Refinement Studies," *Journal of Fluids Engineering*, vol. 116, pp. 405-413, 1994.
- [28] Alicat Scientific, Inc, "Precision Water Flow Meter and Precision Water Flow Controller Operating Manual," no. 32, 2015.
- [29] K.D.Jensen, "Flow Measurements," in *10th Brazillan Congress of Thermal Sciences and Engineering*, Rio de Janeiro, 2004.



## 7 Appendix

### 7.1 Additional J-Nozzle PIV Data

In addition to the velocity profiles just outside the nozzle, profiles at distances of up to 4 pipe diameters away were also measured and can be seen in Figure 54 and Figure 55. As expected the profiles decay however these profiles were not compared to CFD results as CFD historically under predicts jet spreading as mentioned in [25].

The centreline velocity decay curves can be seen for each experiment in Figure 53 below. This curve also gives an indication as to the repeatability of the experiment as if positioning was perfect each curve should lie very close to one another. These results were not compared to CFD results and previous studies such as [25] have found that un-modified two-equation turbulence models under predict the jet decay. These curves however do give some insight into how the jet decays in the near field.

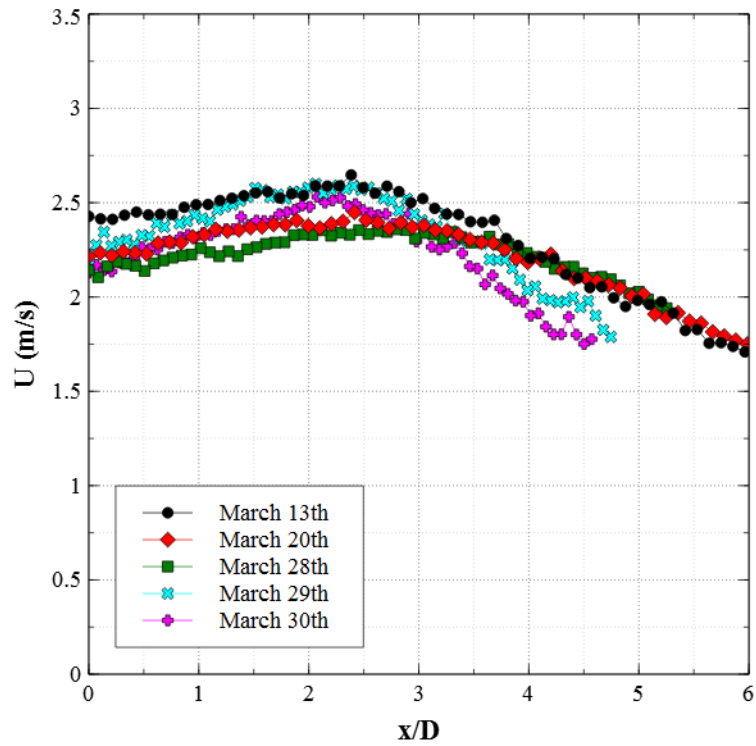


Figure 53: Centreline Velocity Decay for J-Nozzles ( $Q=1.5\text{LPM}$ )

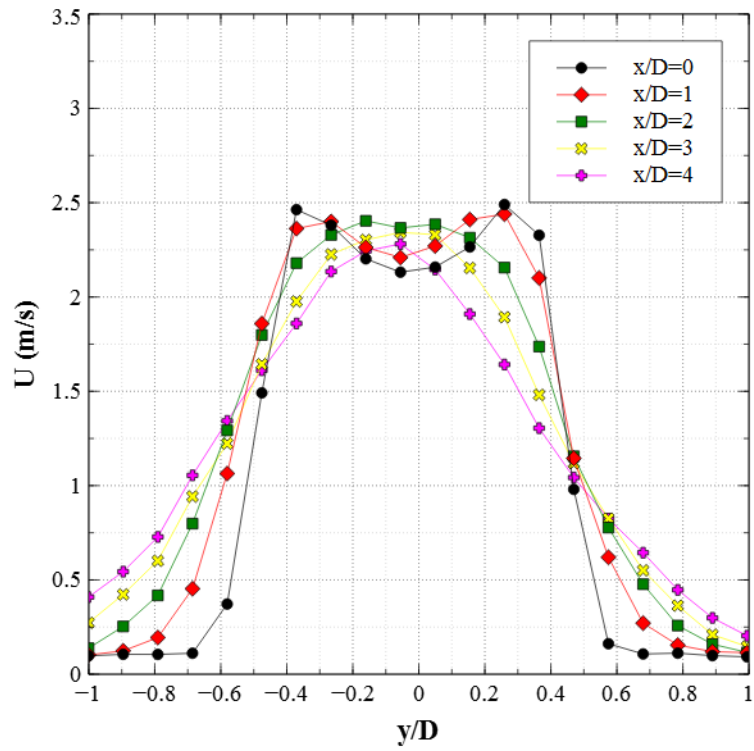


Figure 54: Horizontal Velocity Profiles for March 20th Experiment ( $Q=1.5\text{LPM}$ )

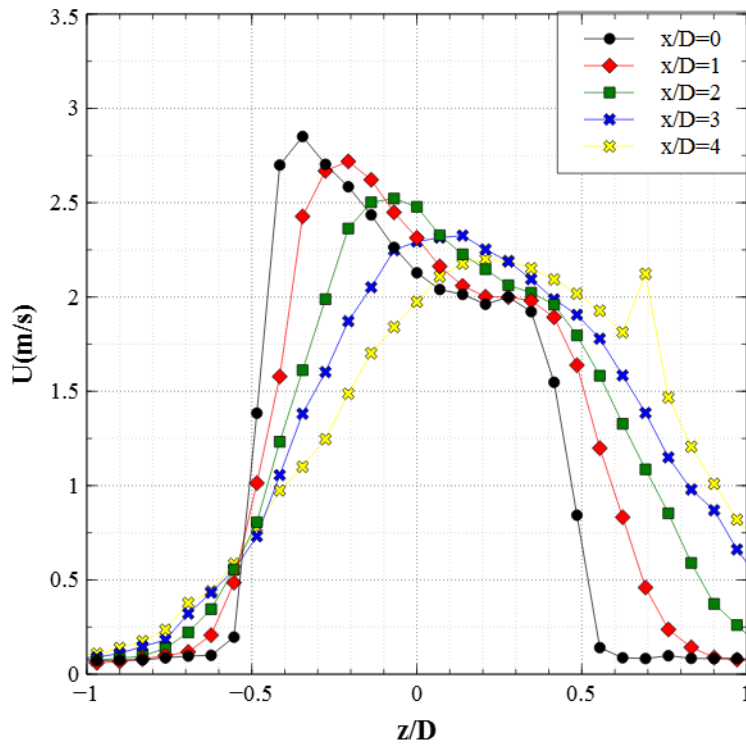


Figure 55: Vertical Velocity Profile for March 30th Experiment ( $Q=1.5\text{LPM}$ )

## 7.2 Experimental Pipe Jet Study

As an experimental benchmark study Particle Image Velocimetry measurements were taken for a round turbulent jet and compared to those of Bougaslawski and Popiel [22]. As the intended method for measuring the velocity field of the J-nozzles is by using PIV, this was intended to serve as a quality check of the data obtained by such experiments.

### 7.2.1 Experimental Setup

The experiment consisted of a 9.398mm ID tube with an entry length of 32 pipe diameters. Using Particle Image Velocimetry the velocity field for the centre of the tube was measured at 4.0LPM and 10 LPM or Reynolds numbers of 10,000 and 25,000.

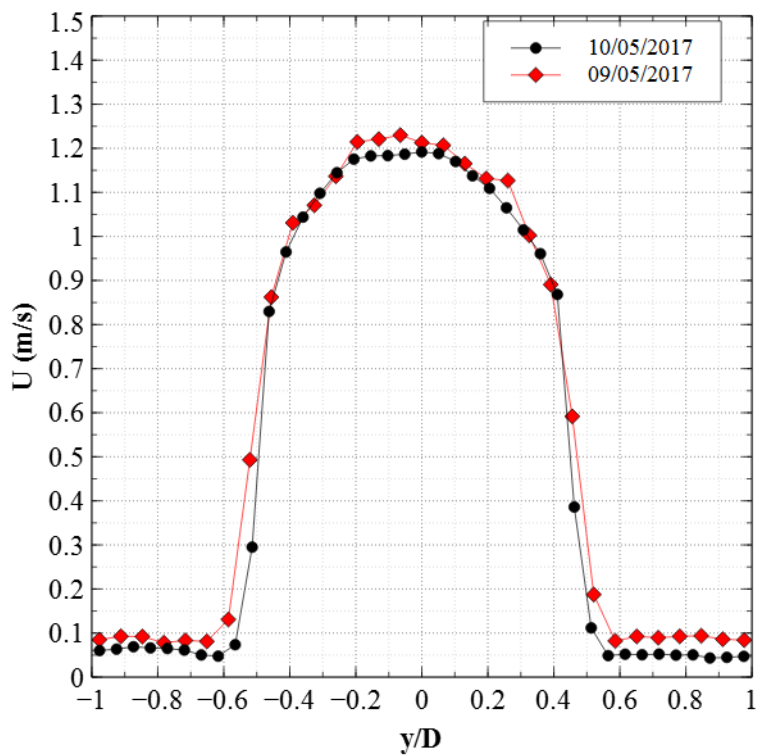


Figure 56: Displays velocity profile at  $x/D=0$  for  $Re=10,000$  ( $Q=4.0$  LPM) and a capture frequency of 500Hz

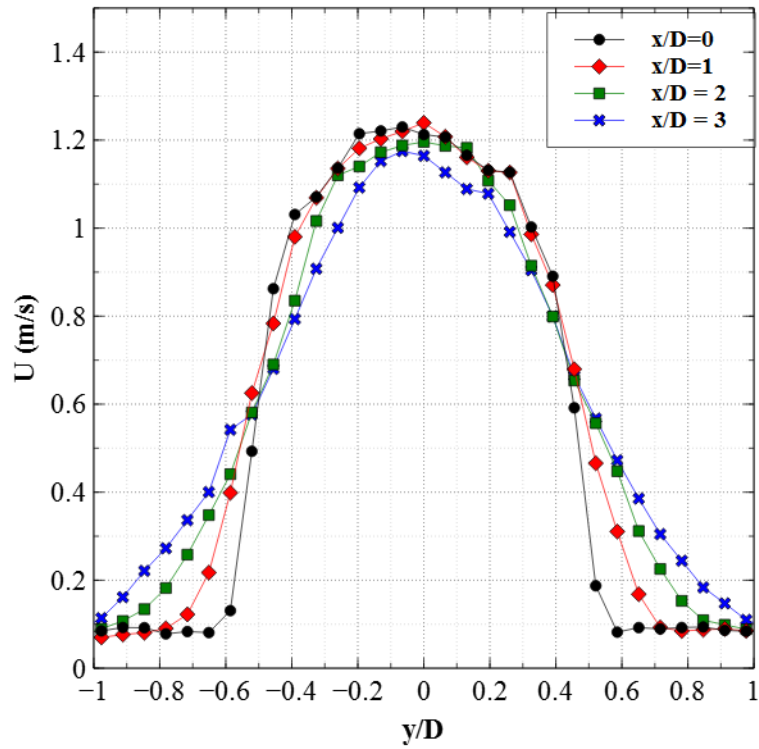


Figure 57: Radial velocity profiles obtained on 09/05/2017 for  $Re=10,000$  ( $Q=4.0$  LPM)

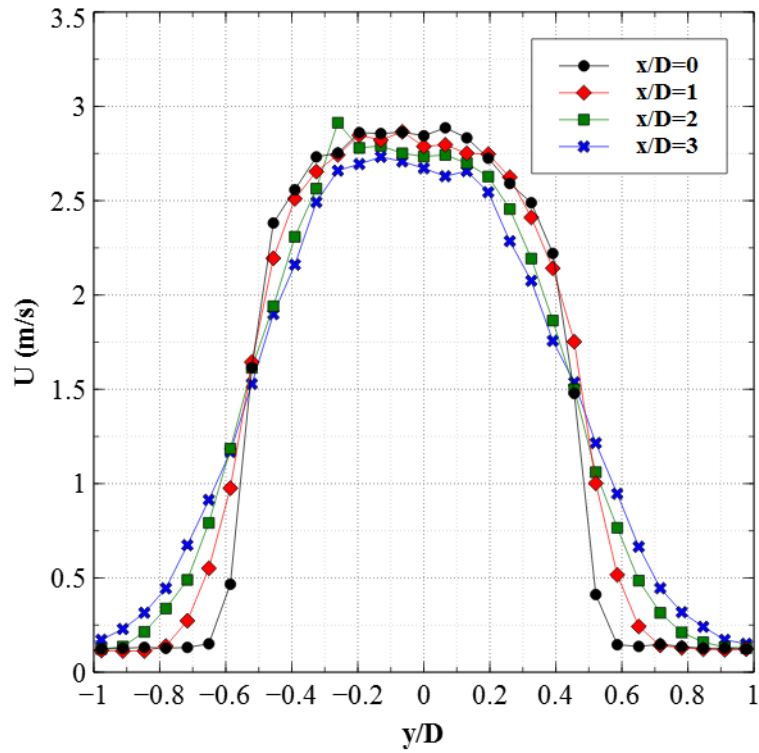


Figure 58: Radial velocity profiles for  $Re=25,000$  ( $Q=10.0$  LPM), obtained on 09/05/2017

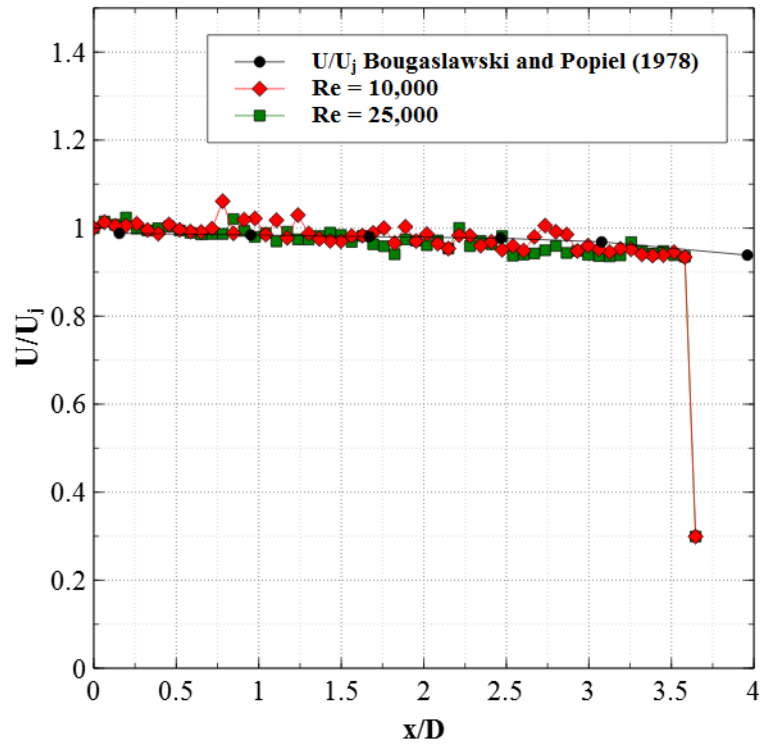


Figure 59: Centreline velocity decay of PIV results compared to Literature

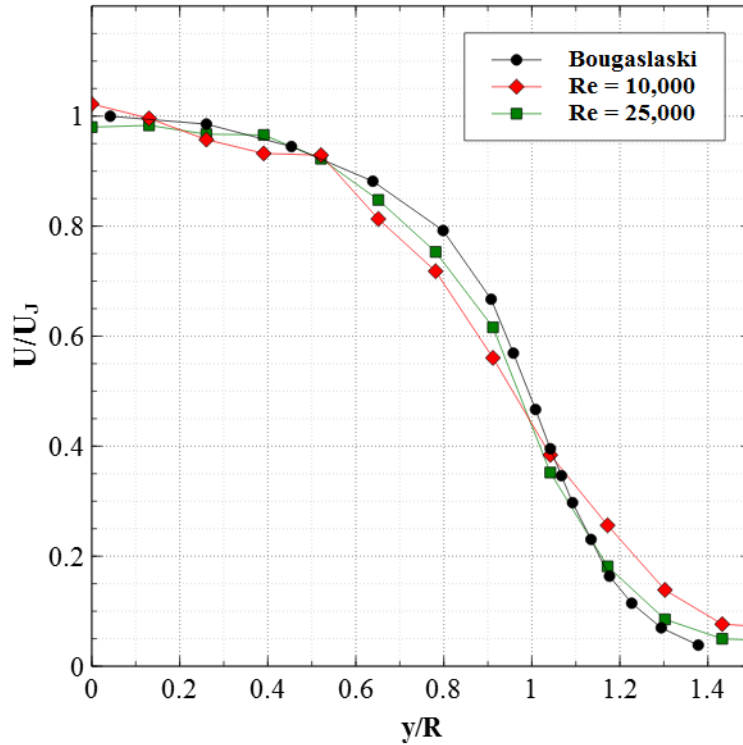


Figure 60: Radial velocity profile from PIV compared to Literature at  $x/D=1$  from the pipe outlet

### 7.3 Header Assembly Drawings

The CAD drawings required to recreate these header assemblies are included in the following section. It should be noted that the scales are not accurate given that the images were resized to fit into this document.

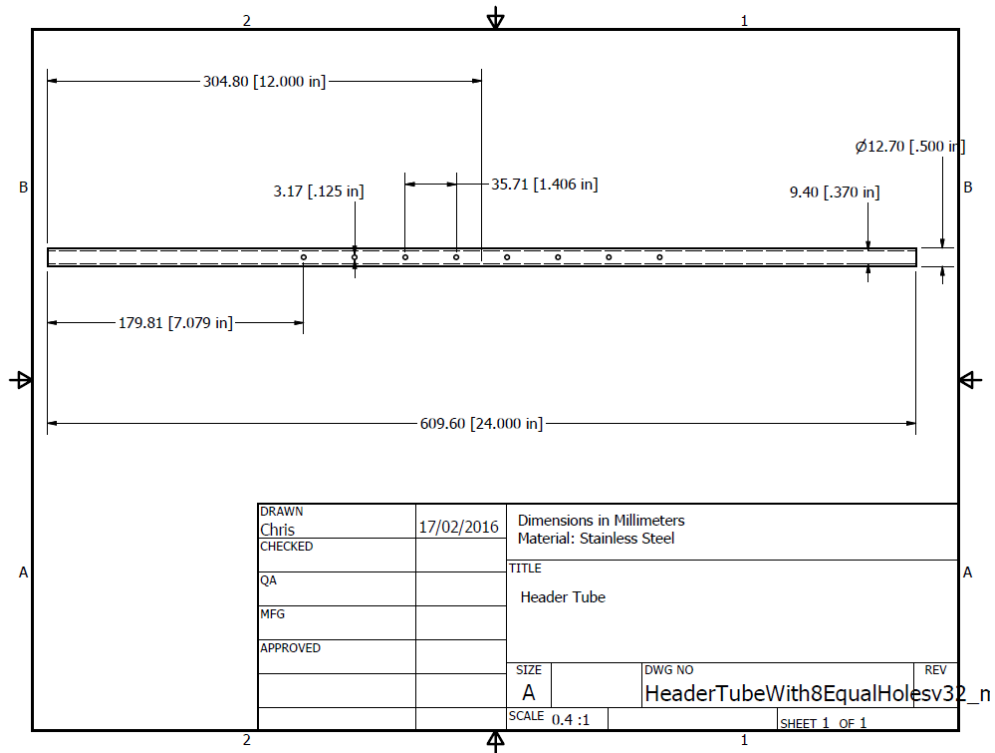


Figure 61: Main Channel Tube with eight locations for discharge ports

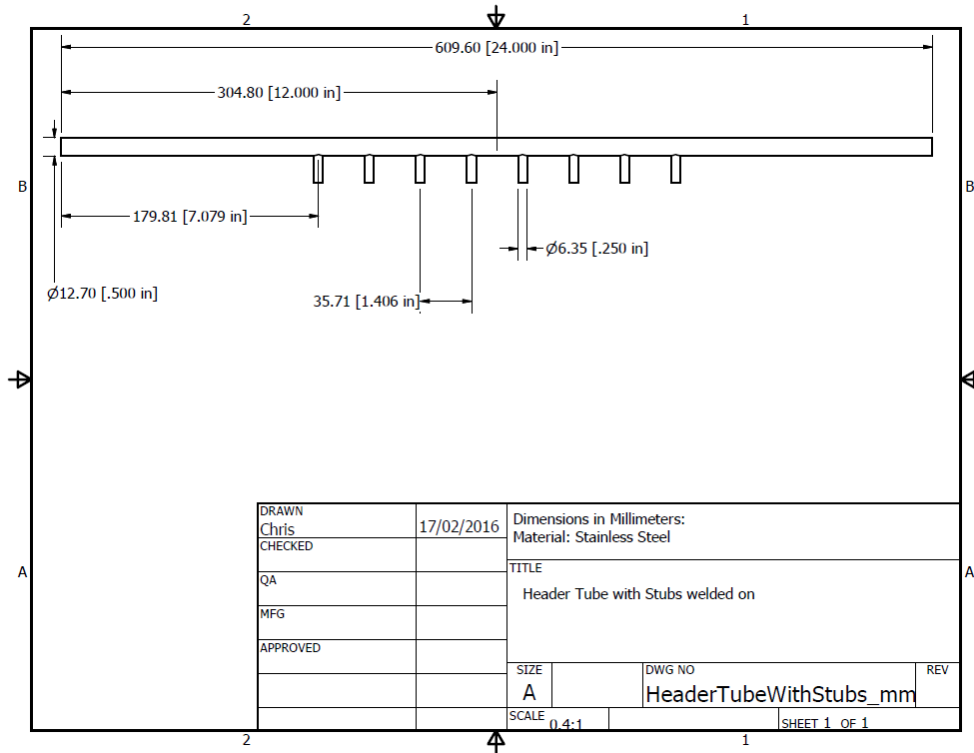


Figure 62: Header Manifold with eight discharge ports

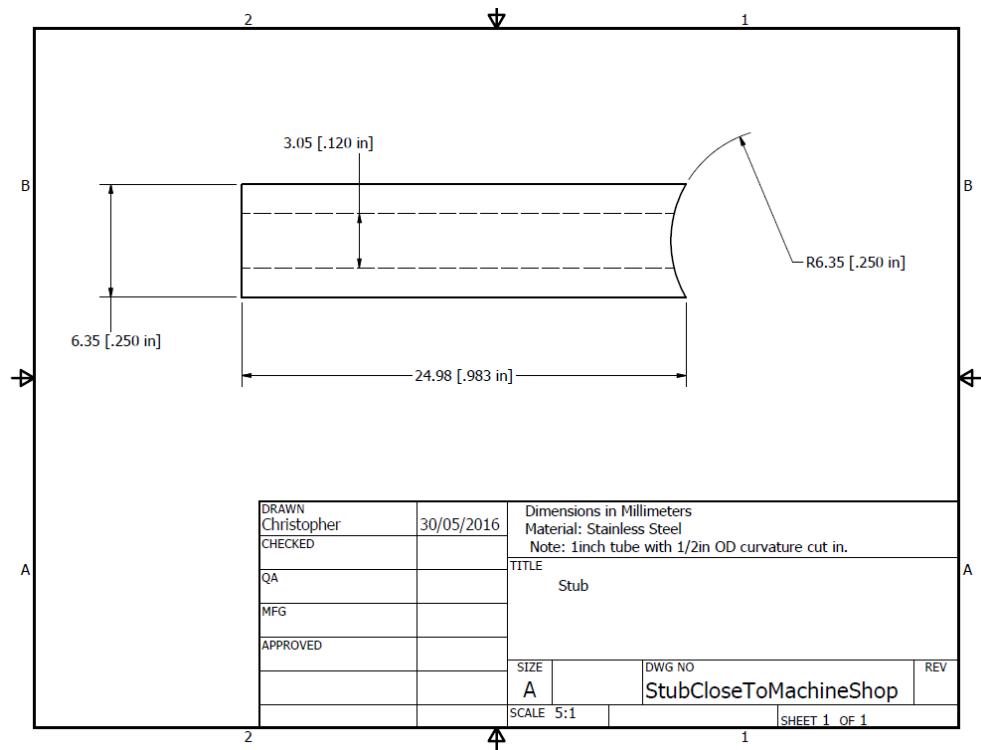


Figure 63: Discharge Port Welded onto main channel

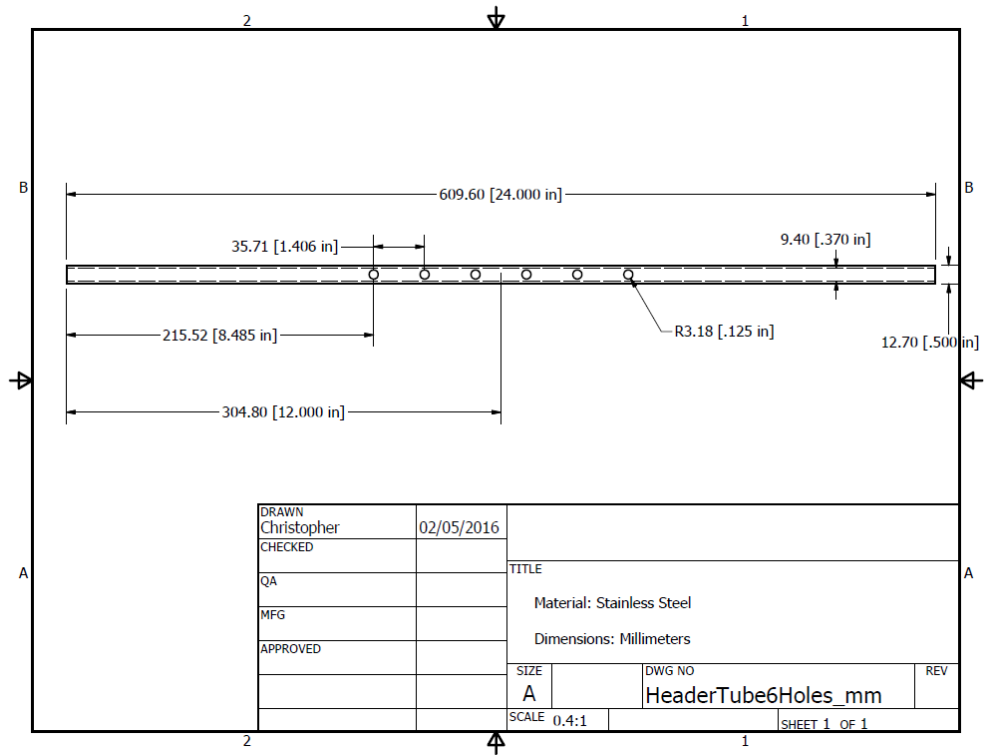


Figure 64: Main Channel for Assembly with six discharge ports locations

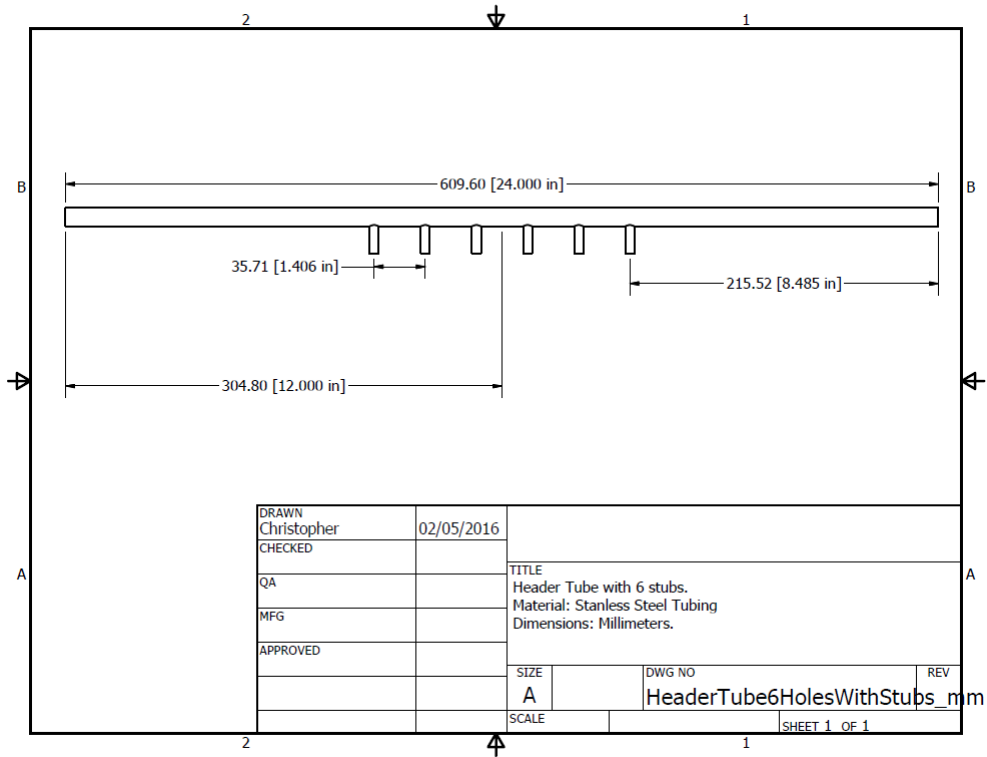


Figure 65: Manifold with six discharge ports

#### 7.4 PIV Standard Operating Procedure

- 1) Place Nozzle in position ensuring that it is orthogonal to the fish tank walls.
- 2) Fill the holding tank and the fish tank until they are both approximately 2/3rds full.
- 3) Setup the camera stand and place the PIV camera on the stand. Ensure that the camera is level.
- 4) Using the PFV software set on low light mode (ensure camera aperture is fully open) adjust camera position until the nozzle is in the desired position in the cameras line of sight.
- 5) Move the lightarm (or laser) into an approximate location such that it will shine near the nozzle and onto the beam stop behind the nozzle.
- 6) Ensure beam stop is in place.
- 7) Place a piece of cardboard with a hole in it over the nozzle. This is to help align the beam in the proper plane as it makes the beam more visible.
- 8) Turn on the laser power supply and turn the system and pump on. This will trigger the pump and chiller in the laser system to turn on. You will notice the outlet temperature of the laser decreasing on the front panel display and the laser will be ready to use once this reaches 22°C. Once this is reached you should hear 1 or 2 beeps from the laser indicating that it is ready to use.

- 9) Add 6-8 scoops of seed. This amount may need to be modified to allow for 3-6 seed particles per grid spacing.
- 10) Turn the laser energy dials (two of them) all of the way down such that they are both at zero.
- 11) On the front panel display turn “laser” on and “shutter” open. The laser is now on.
- 12) In the INSIGHT software select “Laser On” and “Capture”. You should now be able to see a black screen in the software as the energies are too low to be seen.
- 13) Turn one dial up slowly until the beam is barely visible in the software. There is a delay in the software and this point will likely be overshoot.
- 14) Move the lightarm until the beam appears in the desired plane. Ensure that the beam is as perpendicular as possible.
- 15) If the beam appears too thick it may mean that the lightarm is not aligned properly. One should realign the lightarm as outlined in the manual.
- 16) Remove the beam aligner from the nozzle.
- 17) Turn the laser back on and turn up both laser energies to the maximum.
- 18) Adjust the camera aperture and focus such that there is no glare and the seed is clearly visible.
- 19) Select the option in the insight software which cycles between frames and adjust the laser energies until each frame appears as close as possible in brightness. This is to ensure that no seed is lost between frames.

- 20) Turn Off laser
- 21) Turn on the pump and alter the flow rate until it is roughly the needed value.
- 22) Turn the laser back on and take 1 image at a time. Process this image to test your timing setup. In particular we are trying to tune our delta t (the time between frames). We want this value to be such that 1 seed particle moves a maximum of  $\frac{1}{4}$  of a grid spacing or 3-4 pixels. Another way to check this value is to click under TOOLS on VECTORS and then VECTOR STATISTICS. This will give the percentage of good and bad vectors. Aim for 90% of the vectors to be good. It should be noted that if there are high gradients it may be very difficult to achieve this.
- 23) Turn the laser off.
- 24) Turn the capture mode from “Continuous” to “Sequence” and select the number of captures you want to take. One capture comprises two frames and one set of velocity measurements. Select an appropriate amount of captures based on your capture frequency and the desired amount of time you want to sample the flow over.
- 25) Turn the laser back on and adjust the pump frequency until the desired flow rate is achieved. Ensure that it is stable at this flow.
- 26) Once that has been achieved hit “Laser On” and “Capture”. This will trigger the system to begin collecting data and you will see the images appear on the screen. It must be noted that the system takes longer to

display these images than it does capturing them. This means that after the expected amount of time for the measurements has elapsed, you can turn the laser off without affecting your data.

27) Turn the laser off.

28) Move to the processing tab and create an appropriate spatial calibration.

Make sure that the processing grid used matches with the delta t used to ensure good quality data. Refer to the INSIGHT manual for more information into processing and post processing.

29) After the processing is done open TEC PLOT. By default it should open the last image processed and show its velocity field. Note, the scale might be off due to 1 bad vector.

30) Select all of the files processed and open them in this instance of TEC PLOT. Then in the small window select the “Compute Average Field” option. This will compute the average velocity field over all of the images selected.

31) To output this data select File->Write Data File. It is recommended that ASCII and POINT are selected instead of BINARY and BLOCK. This will output the selected data as a .dat file.